

On the Detectability and Use of Normal Modes for Determining Interior Structure of Mars

Felix Bissig¹ · Amir Khan¹ · Martin van Driel¹ · Simon C. Stähler¹ ·
Domenico Giardini¹ · Mark Panning² · Mélanie Drilleau³ · Philippe Lognonné³ ·
Tamara V. Gudkova⁴ · Vladimir N. Zharkov⁴ · Ana-Catalina Plesa⁵ ·
William B. Banerdt²

Received: 22 June 2018 / Accepted: 2 October 2018 / Published online: 18 October 2018
© Springer Nature B.V. 2018

Abstract The InSight mission to Mars is well underway and will be the first mission to acquire seismic data from a planet other than Earth. In order to maximise the science return of the InSight data, a multifaceted approach will be needed that seeks to investigate the seismic data from a series of different frequency windows, including body waves, surface waves, and normal modes. Here, we present a methodology based on globally-averaged models that employs the long-period information encoded in the seismic data by looking for fundamental-mode spheroidal oscillations. From a preliminary analysis of the expected signal-to-noise ratio, we find that normal modes should be detectable during nighttime in the frequency range 5–15 mHz. For improved picking of (fundamental) normal modes, we show first that those are equally spaced between 5–15 mHz and then show how this spectral spacing, obtained through autocorrelation of the Fourier-transformed time series can be further employed to select normal mode peaks more consistently. Based on this set of normal-mode spectral frequencies, we proceed to show how this data set can be inverted for

The InSight Mission to Mars II
Edited by William B. Banerdt and Christopher T. Russell

Electronic supplementary material The online version of this article (<https://doi.org/10.1007/s11214-018-0547-9>) contains supplementary material, which is available to authorized users.

✉ F. Bissig
felix.bissig@erdw.ethz.ch

A. Khan
amir.khan@erdw.ethz.ch

¹ Institute of Geophysics, ETH Zürich, Sonneggstrasse 5, 8092 Zürich, Switzerland

² Jet Propulsion Laboratory, California Institute of Technology, 4800 Oak Grove Drive, Pasadena, CA 91109, USA

³ Institut de Physique du Globe de Paris, Univ Paris Diderot-Sorbonne Paris Cité, 35 rue Hélène Brion - Case 7071, Lamarck A, 75205 Paris Cedex 13, France

⁴ Schmidt Institute of Physics of the Earth, Russian Academy of Sciences, Moscow 123242, Russia

⁵ Planetary Physics, Institute of Planetary Research, German Aerospace Center (DLR), Rutherfordstraße 2, Berlin 12489, Germany

globally-averaged models of interior structure (to a depth of ~ 250 km), while simultaneously using the resultant synthetically-approximated normal mode peaks to verify the initial peak selection. This procedure can be applied iteratively to produce a “cleaned-up” set of spectral peaks that are ultimately inverted for a “final” interior-structure model. To investigate the effect of three-dimensional (3D) structure on normal mode spectra, we constructed a 3D model of Mars that includes variations in surface and Moho topography and lateral variations in mantle structure and employed this model to compute full 3D waveforms. The resultant time series are converted to spectra and the inter-station variation hereof is compared to the variation in spectra computed using different 1D models. The comparison shows that 3D effects are less significant than the variation incurred by the difference in radial models, which suggests that our 1D approach represents an adequate approximation of the global average structure of Mars.

Keywords Mars · Seismology · Normal modes · Interior structure · Inverse problems

1 Introduction

The NASA InSight mission, which launched on May 5, 2018, will emplace a geophysical package, consisting of a seismometer (SEIS, Lognonné et al. 2012), a heat flow probe (HP³, Spohn et al. 2014) and a transponder for precise tracking (RISE, Folkner et al. 2012), on the surface of Mars at the end of November 2018. The goals of the mission are to provide insight on formation and evolution of Mars by investigating interior structure and processes of Mars (Banerdt et al. 2013). To achieve this, InSight will make use of advanced single-seismometer analysis techniques (e.g., Panning et al. 2015; Khan et al. 2016; Böse et al. 2017; Panning et al. 2017), along with extremely precise measurements of variations in the spin axis of the planet (Folkner et al. 2012), and the subsurface thermal gradient (Spohn et al. 2014), to provide the first direct measurements of the internal structure of Mars, including thickness, structure and composition of crust, mantle and core, thermal state of the interior, rate and distribution of internal seismic activity, and rate of meteorite impacts.

InSight will be the first dedicated extraterrestrial seismology mission to study the interior of Mars. While the Viking missions carried seismometers to Mars in the mid-1970s, the seismometers were fixed on the lander, which, because of wind-induced lander shaking, precluded the unambiguous detection of events (Anderson et al. 1977; Solomon et al. 1991; Lorenz et al. 2017). The SEIS experiment onboard InSight (Lognonné et al. 2012) consists of a very broadband seismometer (in addition to a short-period seismometer) that will be deployed on the ground and should enable detection of the normal modes of Mars, i.e., the very long-period signal associated with the finite frequency response of the planet to an excitation (marsquake). The advantage of using normal modes to estimate the globally averaged 1D structure is that these are independent of the excitation mechanism, i.e., epicenter location and origin time are not required (excitation mechanism and epicentral distance only cause a relative modulation of eigenfrequency-amplitudes).

Normal mode seismology on the planets has been discussed before in the context of the Apollo lunar seismic data (Carr and Kovach 1962; Derr 1969; Gudkova and Zharkov 2000, 2001, 2002; Gudkova et al. 2011; Gudkova and Raevskii 2013; Khan and Mosegaard 2001; Gagnepain-Beyneix et al. 2006), in the framework of theoretical and pre-mission science studies on Mars (e.g., Bolt and Derr 1969; Okal and Anderson 1978; Gudkova et al. 1993; Lognonné and Mosser 1993; Gudkova and Zharkov 1996; Lognonné et al. 1996; Kobayashi and Nishida 1998; Gudkova and Zharkov 2004; Lognonné and Johnson 2014; Zheng et al.

2015; Lognonné et al. 2016; Zharkov et al. 2017; Schimmel et al. 2018) and on the giant planets (Vorontsov et al. 1976; Lognonné and Mosser 1993; Lognonné et al. 1994; Gudkova et al. 1995; Gudkova and Zharkov 2006; Gaulme et al. 2015). In the context of InSight, the feasibility of spectral estimation and inversion of fundamental mode eigenfrequencies has been illustrated by Panning et al. (2017), who found, based on seismometer response, current expectations for lander-generated, wind-induced pressure, and temperature noise that detection of normal modes in the frequency range 5–25 mHz should be possible during nighttime. The inversion showed that structure down to a depth of ~ 250 km, comprising crust, lithosphere and uppermost mantle, could be constrained.

In this study we build upon and extend the findings of Panning et al. (2017) by first showing that it is possible to extract a single “observable” related to the normal mode spectral spacing following an earlier suggestion of Okal and Anderson (1978) that the spacing between fundamental modes is expected to be constant in a certain frequency range because of a relatively constant phase velocity on Mars. Secondly, we employ the information contained in the spectral spacing to reliably pick fundamental-mode peaks and invert these for a globally-averaged structure following the approach of Khan and Mosegaard (2001). In summary, the goal is to test this normal mode approach in anticipation of the return of seismic data from Mars. In the following we describe 1) construction of radial reference models; 2) computation of synthetic seismic data; 3) seismic data processing and spectral estimation; 4) the inverse problem, including a synthetic test; and 5) discuss results. Finally, the foregoing is based on radial models and complexities related to three-dimensional (3D) structure (e.g., in the crust and lithosphere) are likely to complicate the analysis. To investigate this in more detail, we conclude with a 3D analysis in a final section.

2 Expected Seismicity and Seismometer Response

There are currently no direct observations of the seismicity of Mars. Instead, seismicity models for Mars are based on geological evidence (e.g., Golombek et al. 1992; Golombek 2002) and simulations of thermal evolution and cooling of the Martian interior (Phillips 1991; Knapmeyer et al. 2006; Plesa et al. 2018). In spite of the apparent absence of detected seismic events during the Viking missions (Anderson et al. 1977; Goins and Lazarewicz 1979), potential sources for seismicity are mainly expected to be meteorite impacts and release of thermal and lithostatic stresses in the form of fracturing. The stresses are visible as faults in images of the Martian surface and topographic data (Knapmeyer et al. 2006; Plesa et al. 2018). Based on these models, the overall seismic moment release is expected to be in the range $3 \cdot 10^{16}$ – $4 \cdot 10^{19}$ Nm over the nominal mission lifetime (Golombek et al. 1992; Knapmeyer et al. 2006; Plesa et al. 2018). The distribution of seismic moment on single events depends on the b-factor in the Gutenberg-Richter law and the largest event that is statistically expected to happen each year (which can make up a considerable amount of the seismic moment budget). Evaluation of all the evidence suggests the occurrence of between 1 and 10 magnitude-5 events with seismic moment around 10^{17} Nm during the nominal lifetime of the experiment (2 Earth years) (e.g., Phillips 1991; Golombek et al. 1992; Knapmeyer et al. 2006; Lognonné and Johnson 2014; Teanby and Wookey 2011; Ceylan et al. 2017; Plesa et al. 2018).

Table 1 compiles the annual occurrence rate for three events based on the fault-derived model of Golombek et al. (1992). The average seismicity expectation of later models is roughly identical to that of Golombek et al. (1992), but the uncertainty is large. For example, Knapmeyer et al. (2006) estimated an uncertainty of around $\pm 10,000\%$ between

Table 1 Occurrence rate of the three events shown in Fig. 1 per nominal mission duration of one Martian year, according to the model by Golombek et al. (1992), based on surface faults and the lower and upper limits of the model by Plesa et al. (2018), which is based on 3D geodynamical simulations. Moments correspond to M_{rr}

| Model | Occurrence rate | | |
|------------------------|----------------------------------|----------------------------------|----------------------------------|
| | $(1 \times 10^{17} \text{ N m})$ | $(3 \times 10^{17} \text{ N m})$ | $(1 \times 10^{18} \text{ N m})$ |
| Golombek et al. (1992) | 1.76 | 0.92 | 0.44 |
| Plesa et al. (2018) | 0.048–36 | 0.024–18 | 0.012–8.4 |

their weakest and strongest model. Plesa et al. (2018) tried to further reduce the uncertainty by considering more “realistic” models obtained from 3D thermal evolution modelling, but were unable to reduce the uncertainty below $\pm 2,000\%$ relative to Golombek et al. (1992) (Table 1).

Given the expected ambient noise level, Lognonné et al. (1996) and Panning et al. (2017) estimated that normal modes should be observable between 5 and 20 mHz for a $M_w 6$ event. Figure 1 shows a comparison between signal amplitudes for a purely radial source located at 10 km depth (epicentral distance of 45°) and the mean noise levels based on an earlier (labeled noise 2016) and the most recent noise model (labeled noise 2017). Noise time series generated from this noise model have been employed throughout for SEIS operation readiness tests and for the MarsQuake Service Blind test (Clinton et al. 2017). It is based on the work of the SEIS noise model working group (Mimoun et al. 2017; Murdoch et al. 2017a,b) and includes proper consideration of the thermal drift of the instrument. The noise model includes contributions from several ambient noise sources due to pressure and magnetic effects, and dust devil-generated reverberations (Kenda et al. 2017). Here, we employ noise time series based on the 2016 mission noise levels, because the prediction of this noise is somewhat more conservative. Any improvement in the signal-to-noise ratio in the period range of interest, implies that the proposed method should be applicable to “smaller” magnitude, and therefore more likely, events.

For a $M_w 5.8$ ($M_{rr} = 1 \cdot 10^{18} \text{ N m}$) event, mode peaks should be observable during nighttime from 5–15 mHz and possibly daytime from ~ 10 –15 mHz. For a $M_w 5.5$ ($M_{rr} = 3 \cdot 10^{17} \text{ N m}$) event, normal modes could possibly be detectable in the range ~ 10 –15 mHz, whereas for a $M_w 5.2$ ($M_{rr} = 10^{17} \text{ N m}$) event, mode peaks are unlikely to be detected.

3 Methods: Forward Problem

3.1 Overview

In the following we briefly describe the methodology summarised and illustrated in Fig. 2. We have broadly divided the strategy into four main stages (colour coded).

Input (white box): In the absence of seismic data from Mars, the input stage consists of computing representative seismic waveforms (Sect. 3.3) based on physically realistic models of the interior structure of Mars (Sect. 3.2). For increased complexity, waveforms are combined with realistic noise to produce the equivalent of “real” (synthetic) Martian seismograms.

Processing (blue boxes): A spectrum is computed for each seismogram via Fast Fourier Transform (FFT; light blue) (Sect. 3.4). From the spectrum we compute the autocorrelation

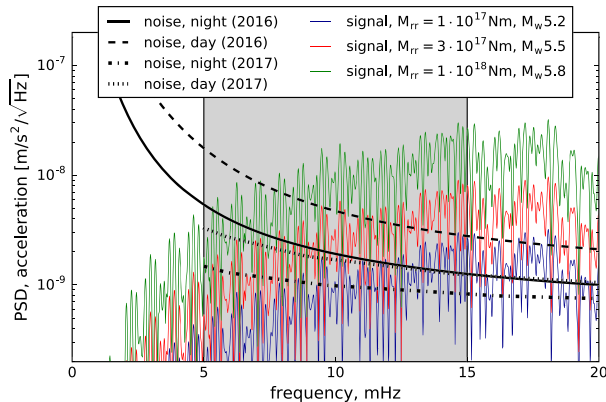


Fig. 1 Power spectral density for three different magnitude events of which 1–10 are expected to occur during the nominal mission lifetime (2 years), compared to the expected ambient noise level from instrument, barometric pressure, and magnetic fields during daytime (dashed line) and nighttime (solid line). The dotted line shows the pure instrument self-noise level, which may be obtained by decorrelation of recorded pressure and magnetic field from the seismic record (Murdoch et al. 2017a). The two noise response curves are both based on the work of the InSight noise model working group (Murdoch et al. 2017a,b; Mimoun et al. 2017). The grey area marks the frequency range of interest

to obtain the spectral spacing (blue). We then use the spacing to identify fundamental-mode spectral peaks (dark blue).

Inversion (red boxes): Those represent the inversion stage, where spectral peaks are inverted for interior structure (Sect. 4). In a preliminary inversion (light red), model fits are checked to ensure that all identified spectral peaks are properly assigned. Mis-assigned peaks are labeled as outliers and removed from the data (red), whereas initially unassigned peaks can, based on data fit, be added to the data set. The inversion is repeated to produce a set of “final” models of the interior structure of Mars (Sects. 3.4.2 and 4.1).

Reiteration (yellow box): The entire procedure (input, processing, and inversion) is run repeatedly as new data come in and previous models are updated.

The method is illustrated for a single relatively large ($M_{rr} = 10^{18}$ Nm) shallow (10 km depth) event, which based on Fig. 1, is expected to be large enough to result in the detectable excitation of normal modes throughout the frequency band of interest.

3.2 Generating Seismic Models

In constructing interior structure models of Mars we rely on a unified description of the elasticity and phase equilibria of multicomponent, multiphase assemblages from which mineralogical and P- and S-wave speed (V_P and V_S) and density (ρ) models as functions of pressure (depth) and temperature are constructed. For this purpose, we employ the free-energy minimization strategy described by Connolly (2009) that predicts rock mineralogy, elastic moduli, and density along self-consistently computed mantle adiabats for a given bulk composition. The thermodynamic formulation of Stixrude and Lithgow-Bertelloni (2005) with parameters as in Stixrude and Lithgow-Bertelloni (2011) are employed. To estimate bulk rock from single mineral properties we use Voigt-Reuss-Hill (VRH) averaging. Pressure is obtained by integration of the load from the surface. Mantle compositions are explored within the $\text{Na}_2\text{O}-\text{CaO}-\text{FeO}-\text{MgO}-\text{Al}_2\text{O}_3-\text{SiO}_2$ (NCFMAS) model chemical system.

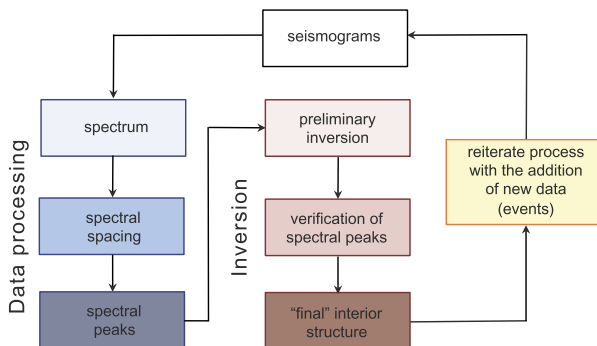


Fig. 2 Normal mode data processing and inversion scheme. Input (white box) consists of synthetically computed seismograms (this study) but will be replaced with proper data as these become available. Processing (blue boxes) relies on spectral estimation in the form of computation of the autocorrelation of the spectrum to determine the frequency spacing which is applied to select peaks (frequencies) corresponding to normal modes. In the inversion (red boxes) the selected spectral peaks are inverted for globally-averaged interior structure models. Finally, the entire procedure is reiterated (yellow box) with the availability of additional data

This model accounts for > 98% of the mass of the mantle in the experimental Martian model of Bertka and Fei (1997).

Information on the mantle composition of Mars come from geochemical analyses of Martian meteorites (e.g., Dreibus and Wänke 1985; Treiman 1986; McSween 1994; Taylor 2013). In the model of Taylor (2013), which is adopted as reference model in this study, the mantle is found to contain 18.7 wt% FeO implying a Martian mantle Mg# of ~ 73 ($100 \times \text{molar Mg/Mg + Fe}$), in comparison to the magnesium-rich terrestrial upper mantle value of ~ 90 (e.g., McDonough and Sun 1995; Lyubetskaya and Korenaga 2007). This and other chemical models are discussed in more detail by Khan et al. (2018). The sublithospheric mantle is assumed to be compositionally uniform. In the crust, we rely on the model of Taylor and McLennan (2009). In the lithosphere, we compute temperature using a linear gradient, which is determined from the surface temperature (273 K) and the temperature (1573 K) at the bottom of the lithosphere (190 km depth). The bottom of the lithosphere is defined by the intersection of the conductive geotherm and the mantle adiabat. The sublithospheric mantle adiabat is defined by the entropy of the lithology at the temperature at the base of the lithosphere. In the crust, we follow Khan et al. (2018) and reduce the seismic properties by multiplying by a constant porosity factor of 0.6, which increases linearly to 1 at the bottom of the crust. Due to lack of sensitivity, core parameters are unimportant.

To incorporate effects of anelasticity, we follow the approach of Nimmo and Faul (2013) as implemented in Khan et al. (2018), who employed the laboratory-based viscoelastic model (extended Burgers) of Jackson and Faul (2010). This viscoelastic model is based on laboratory experiments of torsional forced oscillation data on melt-free polycrystalline olivine and is described in detail in Jackson and Faul (2010). However, to simplify matters, we employed a single shear-wave attenuation (Q) model at a reference-period of 1 s and a grain-size of 1 cm. The shear attenuation Q model is fixed to 500 and 150 in the crust and upper mantle, respectively, after Zharkov et al. (2017) and Khan et al. (2018). As for the frequency dependence (α) of Q , Khan et al. (2018) obtained Q values at periods of 1 hr and 1 s of ~ 140 and ~ 150, respectively. This implies a near frequency-independent Q ($\alpha < 0.01$) in the seismic frequency band for the extended Burgers model. We ignore dissipation in bulk ($Q_\kappa = 10^4$) in line with terrestrial applications (e.g., Durek and Ekström

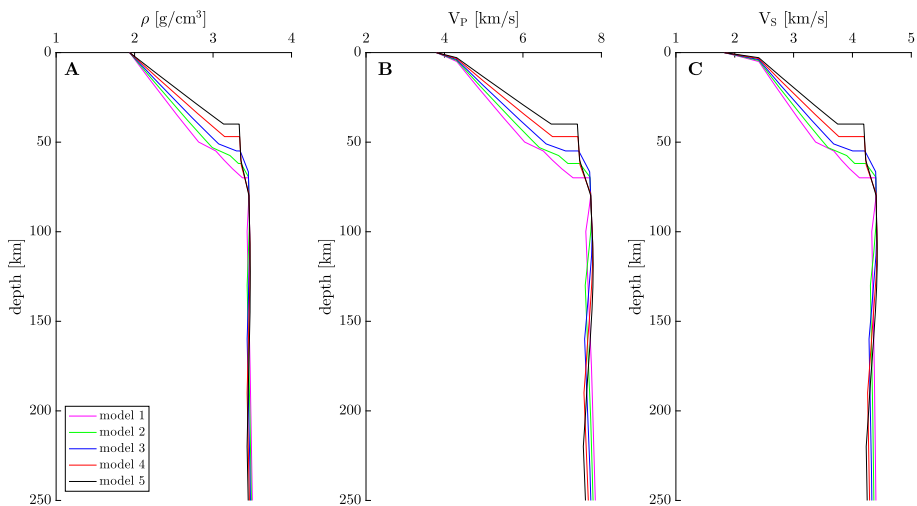


Fig. 3 Radial profiles of density (A) and P-wave (B) and S-wave (C) speed (V_P and V_S) computed for the five models described in Sect. 3.2. Only crust, lithosphere, and upper mantle structure is shown

1996). Radial profiles of isotropic P- and S-wave speeds, and density are shown in Fig. 3 to a depth of 250 km. These models were produced by keeping mantle composition fixed, but varying Moho depth (40–70 km), and temperature (1273–1673 K) and depth (100–220 km) to the bottom of the lithosphere.

3.3 Computing Waveforms and Normal Mode Spectra

We use the full waveform method Yspec of Al-Attar and Woodhouse (2008), which is applicable to spherically symmetric models, to compute synthetic seismic waveforms for the 1D Martian models described previously. The seismograms include the full numerical solution of the visco-elastic wave equation (including attenuation and self-gravitation). Time series were computed in the frequency range 0.2–25 mHz for a purely radial source ($M_{rr} = 10^{18}$ N m) located at 10 km depth and for a length of 8 hours. Effects related to ellipticity and rotation are expected to be small and are ignored (Dahlen and Sailor 1979). Effects arising from lateral variations in crustal properties (e.g., surface and Moho topography, lateral variations in seismic wave speeds and density) will be discussed in Sect. 6.3 (see also Larmat et al. 2008; Bozdağ et al. 2017).

“Realistic” noise is added to the synthetic seismograms using the InSight noise model described earlier in Sect. 2. An example of 4 hours of the resulting three-component synthetic velocity seismograms filtered in the passband 2–25 mHz are shown in Fig. 4 (only the vertical component is shown here since we are only interested in spheroidal modes) at an epicentral distance of 60° for model 4.

To compute amplitude spectra from the time series, we filter these by applying a Butterworth bandpass filter in the frequency range of interest (5–15 mHz). The seismograms are subsequently de-trended, tapered using a cosine-taper, zero-padded and finally Fourier-transformed. Resultant amplitude spectra are also shown in Fig. 4. From the amplitude spectra, we can deduce that detectable signal (spectral peaks) above the background noise level is only present during nighttime and limited to the frequency range 5–25 mHz in line with

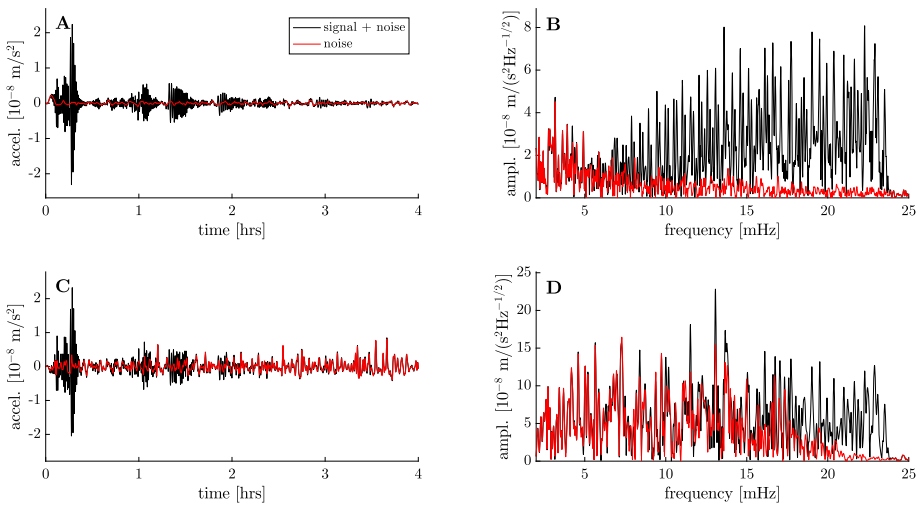


Fig. 4 Synthetic Martian seismograms and amplitude spectra at nighttime (A–B) and daytime (C–D). The waveforms and spectra were computed for model 4 at an epicentral distance of 60 degrees for a M_w 5.8 event ($M_{rr} = 10^{18}$ N m). The noise (red line) is the mean 2016 noise level shown in Fig. 1

the earlier determination of Panning et al. (2017). In reality, we will employ a slightly narrower frequency range 5–15 mHz (see next section). In what follows, we assume that the amplitude spectrum is dominated by fundamental spheroidal modes.

3.4 Spectral Estimation

3.4.1 Spectral Spacing

To extract “observables” from the spectra, we follow an approach based on a suggestion by Okal and Anderson (1978, p. 522, reprinted with permission from Elsevier), who noted that “...the property of relatively constant phase velocities along the fundamental branch might help identify normal modes by using a sequence of them to assign angular orders: A family of modes should closely obey a relation of the form $(l + 1/2)/\omega_l = \text{constant}$. This makes it possible to discriminate between models with otherwise similar periods...”, where l and ω_l denote angular order and associated frequency, respectively. The key to this approach is thus the observation of regularity in spacing of fundamental-mode spectral peaks. This is illustrated in Fig. 5, which shows computed fundamental-mode dispersion curves and frequency spacing (Δf hereinafter) as a function of angular order for the five theoretical models displayed earlier (Fig. 3). Dispersion is found to increase linearly and the associated frequency spacing to be constant, i.e., $\Delta f/\Delta l = \text{constant}$, for angular orders in the range ~ 20 – 80 corresponding to frequencies of 5–15 mHz (gray areas in Fig. 5).

A host of additional globally-averaged models have been investigated. In particular, we examined the change in Δf for five models with larger variation in seismic properties of the uppermost mantle (see Online Resource, Figs. S.1 and S.2). Although qualitatively similar to Fig. 5, the slope of the dispersion curves for each of these models was distinct, but remained, unlike the curves shown in Fig. 5, almost constant across the 5–15 mHz frequency range. As for the models studied presently (Fig. 3), Δf varied by ~ 0.01 (0.158–0.169).

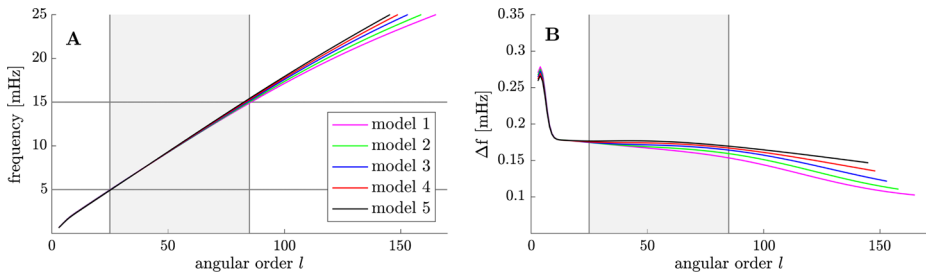


Fig. 5 Computed fundamental-mode dispersion curves (**A**) and frequency spacing (Δf) (**B**) as a function of angular order for the five theoretical models displayed in Fig. 3. Gray areas indicate the region over which the frequency spacing is assumed constant

Proceeding thus to obtain Δf from the data, we compute the autocorrelation of the spectrum, which is shown in Fig. 6A–B (only the positive part of the correlation is shown). Since the spacing is constant, the autocorrelation shows a maximum occurring at Δf and multiples thereof (i.e., at $k \cdot \Delta f$, where k is an integer), which are used to “pick” the “observed” Δf . Figure 6A–B also compares the autocorrelation of the spectrum at nighttime with that at daytime. Clearly, Δf can only be picked during nighttime. To quantify the uncertainty on Δf , we compute the standard deviation using the Δf estimates for all picked peaks. In case only one detectable peak should be present, the width of this peak at half-amplitude will be considered as uncertainty. Picking quality can be improved 1) by rescaling the spectrum with a factor of $1/\omega^k$, such that all peaks within 5 and 15 mHz have similar amplitudes and 2) by restricting computation of the autocorrelation to this frequency range.

As a further test of this method, we computed and plotted the theoretical Δf (using the MINEOS software package (Masters et al. 2011) and linear regression in f - l -space) for all five models shown in Fig. 3 against the picked Δf from the corresponding synthetic waveforms (as described above) for a range of epicentral distances (20° – 160°) during nighttime. The results are plotted in Fig. 6C and the following observations can be made: 1) we obtain a line with a slope ~ 1 as would be expected in case of a perfect match between theoretical and observed predictions of Δf (uncertainties are due to picking errors in Δf for model 4); 2) Δf varies between 0.165–0.176 mHz, but differs for all five models and thereby holds the potential of acting as discriminant between models.

For completeness, we performed the same test on a different event (M_w 5.9) with non-zero moment tensor components ($M_{rr} = 5.426e17$, $M_{r\theta} = 1.174e18$, $M_{r\phi} = -8.5e16$, $M_{\theta\theta} = -3.682e17$, $M_{\theta\phi} = 5.328e17$, $M_{\phi\phi} = -1.744e17$, all numbers in Nm), and located at depths of 10 km, 30 km, and 60 km, respectively. For the 10-km deep source, and for the same range of epicentral distances (20° – 160°) and conditions (nighttime) as for the purely radial source, theoretical and picked Δf are plotted in Fig. 6D. This plot corroborates the results for the purely radial source in the form of a model-dependent frequency spacing, implying that the method also works for more general sources that are not necessarily optimised toward observing spheroidal modes. Similar observations are made for other models and modeled seismic sources (see Online Resource, Fig. S.3).

3.4.2 Spectral Peaks

In the second step of the spectral estimation, we consider the (nighttime) spectral peaks shown in Fig. 4 directly. However, rather than simply picking peaks above a certain threshold, where we potentially run the risk of including peaks related to noise and/or overtones

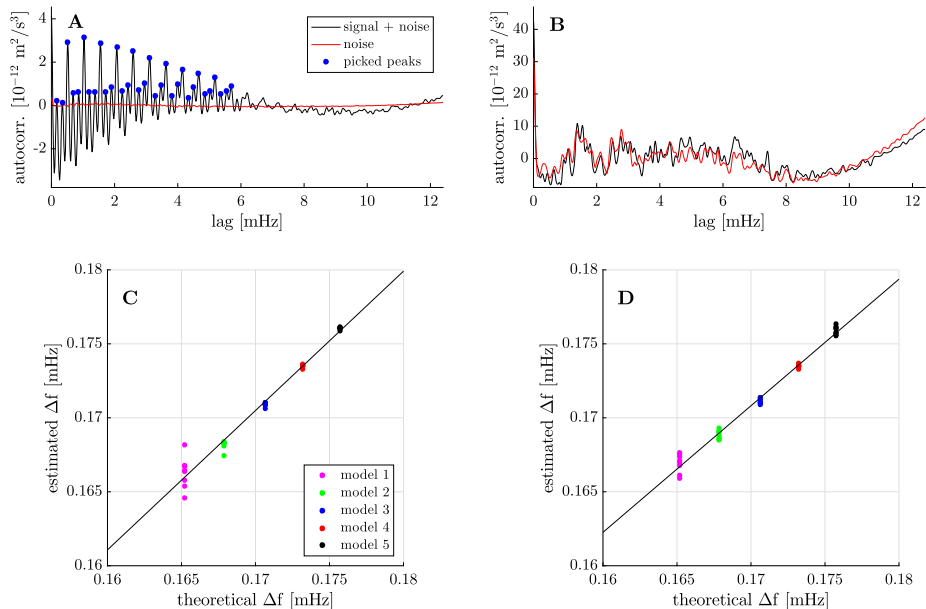


Fig. 6 Autocorrelation of the spectrum for the M_w 5.8 event (purely radial source) and model 4, recorded at 60° epicentral distance and 10 km depth (Fig. 4) during nighttime (**A**) and daytime (**B**) and filtered between 5 and 15 mHz. The regular spacing of normal mode eigenfrequencies is clearly detectable during nighttime. (**C**) Comparison of theoretical and estimated frequency spacing (Δf) for the five radial models shown in Fig. 3 and 8 receivers distributed evenly between 20° and 160° epicentral distance. (**D**) As in (**C**), but for a second M_w 5.9 event with a non-radial source (see main text). Noise (red line) is the mean 2016 noise level shown in Fig. 1

(peaks indicated with empty circles in Fig. 7), we use the information contained in the spectral spacing to assign fundamental-mode spectral peaks. The main idea is to first select a peak (typically we start with a relatively large peak in the middle of the spectrum, e.g., ${}_0S_{54}$) and then to assign neighbouring peaks based on the observed spectral spacing. This method is illustrated in Fig. 7 for noise-free data. The peaks that are picked based on the estimated spacing (blue vertical lines) starting from a given peak are shown with red dots. As a means of verification, we are also showing the theoretically-computed fundamental-mode eigenfrequencies (vertical green lines) for the underlying model (model 4). We observe that between 6.5–12.5 mHz theoretical and estimated eigenfrequencies are in complete agreement, which allows us to correctly assign fundamental-mode peaks. Above and below this frequency range, the blue and green lines differ slightly, suggesting that we are starting to move beyond the straight-line slope indicated in Fig. 5 (gray area). The spectral spacing should be varied within the estimated uncertainty to find the optimal value of Δf that most closely matches a set of spectral peaks. This implies trying different values for Δf (within the estimated uncertainty) across different frequency bands of the spectrum.

The advantage of assigning peaks in this manner is that a significant number of small-amplitude peaks are visibly (empty circles) “out-of-tune” with the estimated spacing. Thus, the observed spectral spacing provides a tool for positively assigning peaks otherwise difficult to label conclusively. It also provides us with a means of identifying and discarding “outliers” (either noise or overtones) that were initially assigned, but could not be fit in the

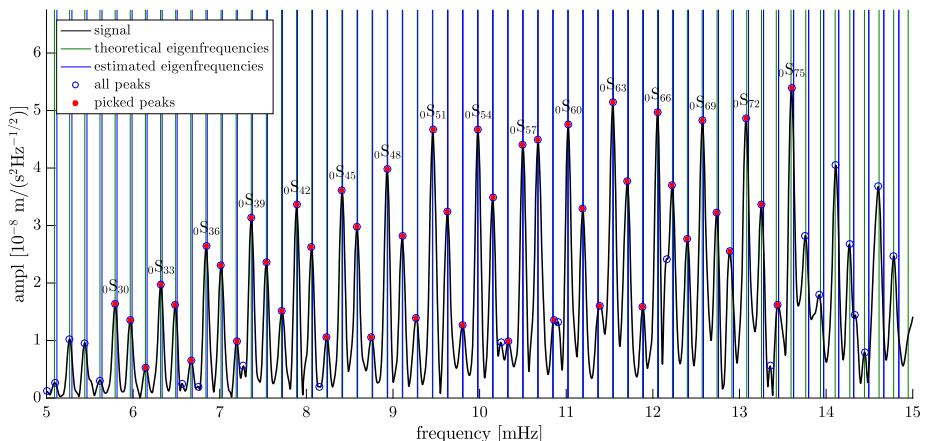
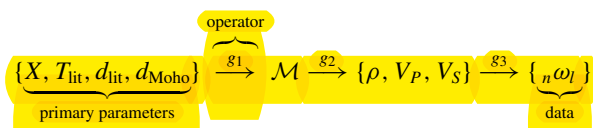


Fig. 7 Noise-free spectrum showing peaks associated with the fundamental spheroidal modes of which some are labeled. For comparison, theoretically-computed and estimated (i.e., selected based on observed frequency spacing) eigenfrequencies are indicated as green and blue vertical lines, respectively. Red dots indicate positively identified fundamental spheroidal mode peaks, whereas open circles identify peaks that have not been selected because of the observed mismatch with the estimated eigenfrequency. This mismatch can be improved by trying to fit different spectral spacings (within the uncertainty of estimated eigenfrequency) across the spectrum. The spectrum is based on model 4

inversion (to be described further in Sect. 5). In addition to these criteria, as a baseline we only pick spectral peaks above a certain threshold amplitude (based on an average pre-event noise level) to ensure that we are above noise level. Since the spectrum in Fig. 7 is noise-free, small-amplitude peaks not identified as fundamental modes have to correspond to overtones and their contribution to the autocorrelation is invariably negligible. When physical noise is added, overtones are not unambiguously identifiable and are hence treated as noise.

3.5 Forward Problem Summary

The forward model consists of computing fundamental-mode spectral frequencies given a model of the interior structure of the crust and thermochemical structure of mantle (this includes the core but because of lack of sensitivity we abstain from discussing core-related aspects). To determine stable mineralogy (\mathcal{M}), isotropic shear (V_S) and compressional (V_P) wave speeds, and density (ρ) along self-consistent mantle adiabats, we employ, as described in Sect. 3.2, Gibbs free-energy minimization. Based hereupon, we can summarize the forward problem in the form of the following modeling scheme



where the primary parameters are described in Sect. 3.2 and (\mathcal{M}, V_S, V_P) are secondary parameters that are required for the purpose of computing fundamental-mode spheroidal eigenfrequencies ${}_n\omega_l$ where n and l designate mode number and angular order, respectively (Sect. 3.4). The operators (g_1, \dots, g_3) describe the Gibbs free-energy minimization, equation-of-state modeling, and spectral estimation problems, respectively. Model parameters and forward operators are summarised in Table 2.

Table 2 Model and data parameters, prior range (prior information), and forward model operators. Note that we only invert for primary parameters; secondary parameters are conditional, i.e., depend on primary parameters. Primary parameters are all uniformly distributed

| Model parameters (primary) | Prior range | Description |
|------------------------------|----------------------------|---|
| ϕ_0 | 0.6 | Crustal porosity (fixed) |
| T_{surface} | 273 K | Surface temperature (fixed) |
| T_{lit} | 1373–1773 K | Adiabatic temperature at d_{lit} |
| d_{Moho} | 10–100 km | Moho thickness |
| d_{lit} | 100–300 km | Depth to conductive geotherm-adiabat crossing |
| X_{cr} | Taylor and McLennan (2009) | NCFMAS crustal composition (fixed) |
| X_m | Taylor (2013) | NCFMAS mantle composition (fixed) |
| R_{core} | 1765 km | Core radius (fixed) |
| X_S | 21 wt% | Core Sulphur content (fixed) |
| Q_μ | | Shear attenuation (fixed) |
| Model parameters (secondary) | | |
| \mathcal{M} | | Equilibrium mineralogy |
| V_P, V_S | | Isotropic (anelastically-corrected) P- and S-wave speed |
| ρ | | Density |
| Data | | |
| $n\omega_l$ | | Fundamental-mode eigenfrequencies |
| Method | | |
| g_1 | | Thermodynamic modeling |
| g_2 | | Equation-of-state modeling |
| g_3 | | Prediction of normal mode eigenfrequencies |

4 Methods: Inverse Problem

To solve the inverse problem $\mathbf{d} = g(\mathbf{m})$, where \mathbf{d} is a data vector consisting of observations ($n\omega_l$) and g is an operator that maps from the model space into the data space (see forward modeling scheme above), we employ a Bayesian approach (e.g., Mosegaard and Tarantola 1995)

$$\sigma(\mathbf{m}) = k \cdot f(\mathbf{m}) \mathcal{L}(\mathbf{m}), \quad (1)$$

where $f(\mathbf{m})$ is the prior model parameter probability distribution, $\mathcal{L}(\mathbf{m})$ is the likelihood function, which measures the misfit between observed and predicted data, k is a normalization constant, and $\sigma(\mathbf{m})$ is the posterior model parameter distribution and the solution to the inverse problem.

The Metropolis algorithm is employed to sample the posterior distribution (Eq. (1)) in the model space (Mosegaard and Tarantola 1995). This algorithm is an importance sampling algorithm that ensures that models that fit data well and are simultaneously consistent with prior information are sampled more frequently. The Metropolis algorithm samples the model space with a sampling density that is proportional to the (target) posterior probability density and thus ensures that low-probability areas are sampled less excessively. This is an important feature of any algorithm that wishes to randomly sample high-dimensional model spaces where the probability density over large proportions of the volume are near-zero.

The intervals within which the primary parameters (Table 2) are sampled are uniformly distributed. This prior information ($f(\mathbf{m})$ in Eq. (1)) represents a “minimal prior” that samples wide ranges for the individual parameters with bounds set by various laboratory measurements and previous inversion results (e.g., Nimmo and Faul 2013; Khan et al. 2018). Upper and lower limits on model parameter ranges are summarized in Table 2 and, for reference, are larger than InSight mission requirements ($\pm 5\%$ for S-wave speed).

4.1 Computing the Misfit Function

To compute the likelihood function in Eq. (1), we have to define a misfit criterion between observed and synthetically-computed fundamental-mode eigenfrequencies. This would be trivial for the case where we could assign individual peaks with a fundamental spheroidal mode label (${}_nS_l$). However, this information is not available and we have to resort to a different approach where a computed catalogue of fundamental spheroidal modes in the frequency range 5–15 mHz are fit to the frequencies of the observed (regularly-spaced) peaks. The problem is further compounded by absence of information on focal mechanism, which precludes determining synthetic amplitudes using waveform modeling or normal mode summation techniques, for example.

In this study, we use the method of Khan and Mosegaard (2001) who fitted lunar free oscillation periods in the following manner. The main idea resides in creating a synthetic spectrum for a given interior-structure model based on the eigenfrequencies for that particular model and the observed spectrum and then to compare the latter with the so-computed synthetic spectrum to obtain the likelihood function (misfit)

$$\mathcal{L}(\mathbf{m}) \propto \exp\left(-\sum_l \frac{\|A_{\text{obs}}(0\omega_l) - A_{\text{syn}}(0\omega_l)\|^2}{2\sigma_l^2}\right), \quad (2)$$

where $A_{\text{obs}}(0\omega_l)$ and $A_{\text{syn}}(0\omega_l)$ are the amplitudes of the observed and synthetic spectrum at the observed frequency $0\omega_l$, respectively, and σ_l is the uncertainty on the spectral amplitude of mode l . An example of a synthetic spectrum (to be discussed further below) is illustrated in Fig. 8. While difficult to estimate accurately, a conservative value for σ_l chosen here is $\pm 30\%$ of the observed value. In summary, models that result in calculated spectral peaks that match the observed spectral peaks are more likely to be sampled than others.

We compute synthetic spectra by a superposition of functions of the form $k/(1+k'\omega^2)$ (black line in Fig. 8), where $k = 1$ and $k' = 2500$ and ω is frequency. This implies that for a particular $0\hat{\omega}_{l'}$ (green vertical line in Fig. 8), the optimal amplitude (i.e., the amplitude of the observed spectrum at $0\hat{\omega}_{l'}$) is fitted (intersection of green and red lines in Fig. 8). Based on this optimal amplitude, we can solve $A_{\text{obs}}(0\hat{\omega}_{l'}) = \sum_{l'} \chi_{l'} M_{ll'}$ for the coefficients $\chi_{l'}$, where $M_{ll'} = k/[1+k'(0\hat{\omega}_l - 0\hat{\omega}_{l'})^2]$. This is a linear problem and solved using standard techniques (e.g., Menke 2012). Armed with these $\chi_{l'}$ can now be determined $A_{\text{syn}}(0\omega_l)$ by solving

$$A_{\text{syn}}(0\omega_l) = \sum_{l'} \chi_{l'} \frac{k}{1+k'(0\omega_l - 0\hat{\omega}_{l'})^2} \quad (3)$$

The resultant synthetic spectrum is shown in Fig. 8 (black line) and indicates the value of $A_{\text{syn}}(0\omega_l)$ (intersection of blue and black lines), which is used in determining the misfit (Eq. (2)). With the absence of long uninterrupted recordings from numerous global stations, which are routinely used in terrestrial normal mode studies, the presently computed spectrum is deemed to be an adequate approximation to the “actual” synthetic spectrum. The latter differs from the present $A_{\text{syn}}(0\omega_l)$ by including proper amplitude and phase information,

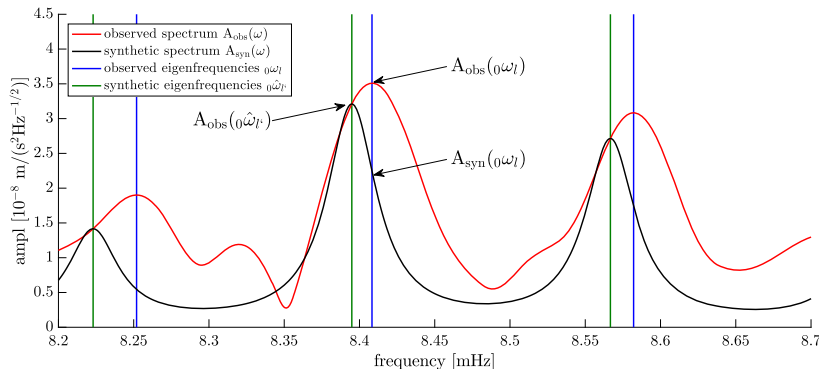


Fig. 8 Illustration of how the synthetic spectrum is constructed from the observed spectrum and the theoretically-computed fundamental-mode frequencies

which, however, implies solving for source mechanism in addition to velocity model (e.g., Gilbert and Dziewonski 1975; Okal et al. 2012; Bogiatzis and Ishii 2014). Finally, k and k' have been chosen so as to approximately reproduce the width of the observed spectral peaks. Changing k and k' affects the resultant misfit in the same manner as varying uncertainty in peak amplitudes, i.e., increasing/decreasing peak width results in a smoother/coarser misfit surface as a result of which broader/narrower probability distributions are obtained.

5 Inversion Results

To test the method, we perform a synthetic inversion following the scheme outlined in Fig. 2. Synthetic data acquisition and processing has already been described. Because of the frequency range considered, we only invert for parameters that are sensitive to crust and upper mantle structure, i.e., temperature at the bottom of and thickness of the lithosphere, and Moho depth (T_{lit} , d_{lit} , and d_{moho}).

5.1 Preliminary Inversion and Spectral Peak Verification

As a first step, we perform a preliminary inversion where all picked fundamental-mode peaks (red and yellow dots in Fig. 9) are inverted. This results in a preliminary set of models and corresponding set of (synthetic) spectra (in gray), which are shown in Fig. 9 and also includes the spectrum for the initial model (in green). Based on this preliminary inversion, we are able to verify our initial selection of peaks and “filter” out those peaks (yellow dots) that are unable to match the fundamental-mode data. This is illustrated in the zoomed-in plots (Fig. 9B–C) where several selected peaks are identified as false (indicated by yellow dots) on account of the consistent mismatch between observed and synthetic spectra (blue peaks), which otherwise provides an excellent fit to the data over the entire frequency range. These “outliers” (related to noise and/or overtones) are subsequently discarded resulting in a “cleaned-up” spectrum (red dots). In addition to removing peaks, we can also employ the preliminary inverted spectra to identify peaks that initially were not selected because the peaks did not match the spectral spacing, but where the synthetically-computed spectral peaks are observed to provide an excellent fit. As an example, after a preliminary inversion, three peaks (green dots) were subsequently identified that qualify as proper peaks (Fig. 9C).

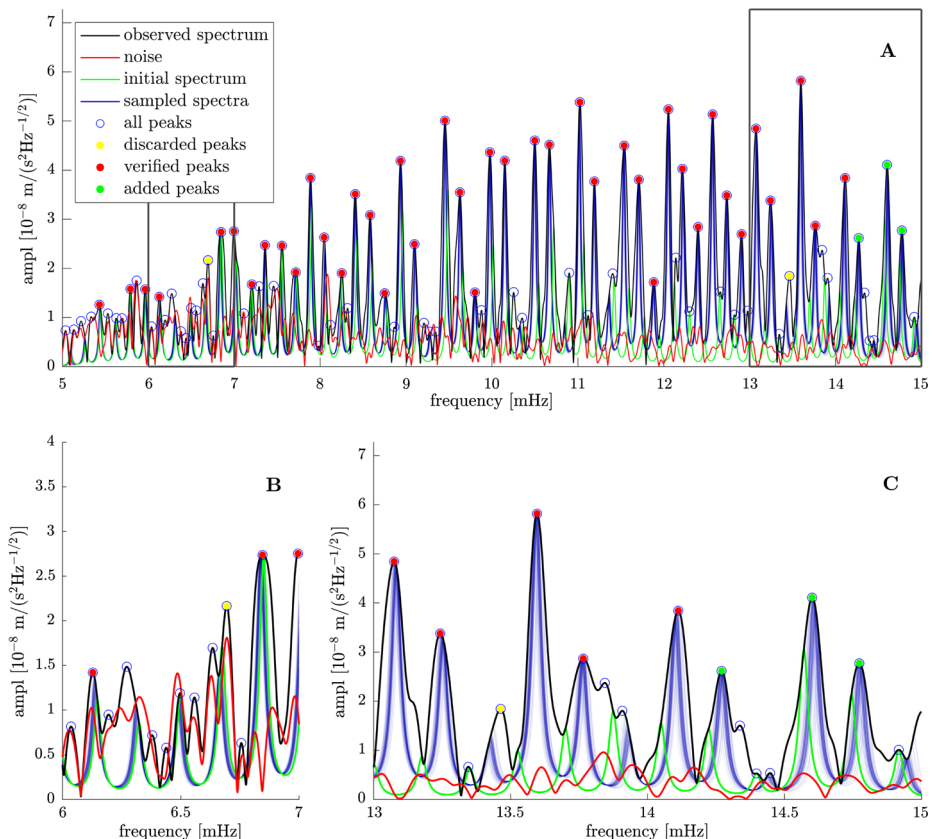


Fig. 9 Example of preliminary data fit (compare blue and black peaks) used for verifying initially-selected peaks (red and yellow dots), including peaks that were not initially selected (green dots). Panels (B) and (C) are zoom-ins of the frequency band (two boxes) shown in panel (A). The noise (red line) is the mean 2016 noise level shown in Fig. 1. The spectrum was computed using model 4

This “new” set of spectral peaks (red and green dots) is now re-inverted to produce a set of “final” models.

5.2 ‘Final’ Inversion

With the removal and addition of signal, the data set is re-inverted for an updated set of interior structure models. Sampled “final” model parameters and seismic profiles are shown in Fig. 10. Both figures indicate that we are generally able to retrieve the “true” model in terms of the main parameters (T_{lit} , d_{lit} , and d_{moho}) in this synthetic test. But it should be clear that because of the assumed uncertainty on peak amplitudes (see Sect. 4.1), a perfect match with the “true” model is not expected. Figure 10 also shows the information gain (cf. histogram widths) that has been obtained through inversion of the “cleaned-up” spectrum relative to prior information (Sect. 4).

While not directly apparent from the seismic profiles (Fig. 10), the depth range to which fundamental modes (${}_0S_{30}$ – ${}_0S_{75}$) in the 5–15 mHz frequency range are sensitive is 0–250 km (see also Panning et al. 2017). In short, the results of this synthetic inversion show the capa-

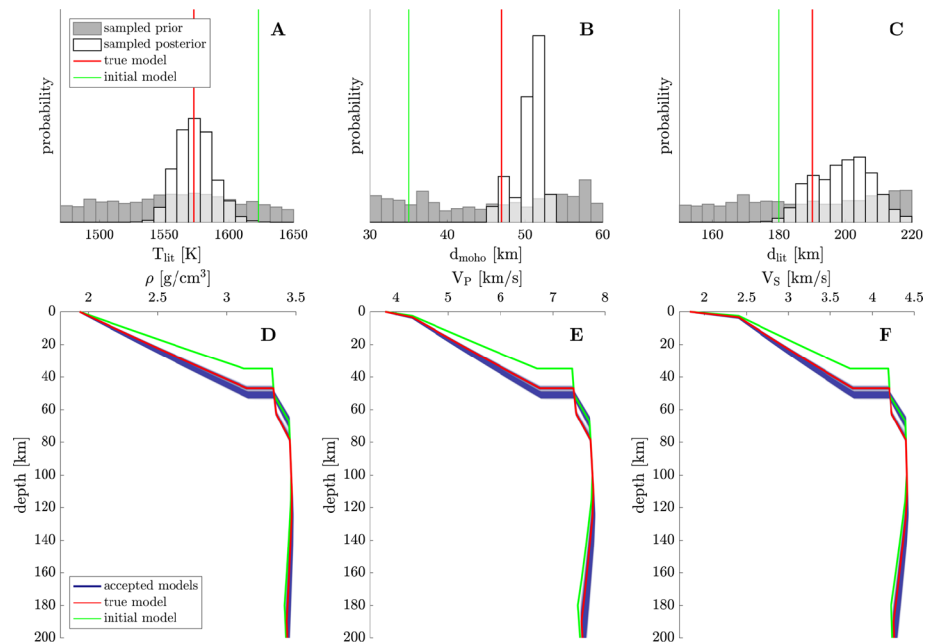


Fig. 10 Sampled prior and posterior distributions for the main crustal and lithospheric parameters of interest. (A) Temperature at the bottom of the lithosphere; (B) Moho thickness; and (C) lithospheric thickness. Corresponding radial profiles of seismic properties in the form of density (D), P-wave speed (E), and S-wave speed (F)

bility of the method to 1) retrieve the sought-for model and 2) to improve results through a data verification stage where picks are consistently checked against the observations for consistency. In case of more complicated spectra, the procedure could be performed repeatedly so as to iteratively refine models and spectra until the desired spectral match is achieved. Finally, as new data become available, we can proceed to update and improve results (final “Reiteration” stage).

Finally, to test the inversion method proposed here, we performed a “full” spectral inversion, i.e., inversion of proper amplitude and phase, assuming a perfectly known source. Results from this inversion (see Appendix A) are similar to those obtained from the present method. This benchmark serves to show that our method is a useful approximation.

6 Application to 3D

6.1 3D Model Construction

To construct a 3D model of Mars’ interior, we generally employ the same methodology outlined in Sect. 3.2, but make a number of modifications by including lateral variations in crust and mantle temperature and surface and Moho topography. Relative to the 1D approach, 3D modeling extensions include a gravity- and topography-based crustal thickness model and a thermal model that derives from thermal evolution simulations of Mars (Plesa et al. 2016). The crustal thickness model is that of Neumann et al. (2004), which assumes a uniform crustal density of 2.9 g/cm³ and average and minimum crustal thicknesses of

40 km and 1 km, respectively. Based on these modifications, we rerun the Gibbs free-energy minimisation pixel-by-pixel, assuming a homogeneous bulk mantle composition. Crust and attenuation model follows the parametrization described in Sect. 3.2. Examples of lateral variations in seismic properties are shown in Fig. 11 in the crust and mantle at depths of 66, 100, and 196 km, respectively.

We would like to note that this 3D model is constructed solely for the purpose of assessing the effects of lateral variations on fundamental spheroidal normal modes. The question of whether this model is realistic is not so relevant in this context. Although the mantle composition is unlikely to be homogeneous on account of geochemical evidence (e.g., Debaillé et al. 2008), the simplifying assumption of constant bulk composition was made purely for computational ease. The variations in the mantle are therefore temperature-dominated, although variations in the crust clearly bear the signature of surface topography. Overall, variations in S-wave speed span a range of the order of $\pm 2\%$, and are probably larger in reality as indicated by Khan et al. (2018), who found variations in S-wave speed of $\pm 4.5\%$ in the crust and $\pm 3.5\%$ at the base of the lithosphere (200–400 km depth).

6.2 3D Waveform Modeling

We use the Salvus software package (Afanasiev et al. 2018) to compute coupled elastic/acoustic wave propagation based on the spectral element method. The mesh respects the surface and Moho topography exactly and is designed to resolve a shortest period of 50 s at one element per wavelength using 4th order basis functions and comprises a total of 221K elements. Waves are propagated for 8 hours with a total of 1.8M time steps. As source we used a vertical dipole (M_{rr}) with a moment magnitude of 10^{18} N m located at the equator at 0° longitude. Receivers were located at the InSight landing site (Mare Elysium) and at additional 100 random locations to allow for statistical analysis. Because we presently only consider a relative comparison between waveforms based on 3D and 1D simulations, we ignore effects due to gravity and attenuation and effectively compute the purely elastic solution. Gravity will be integrated in the near future.

6.3 1D and 3D Normal Mode Comparison

3D waveforms are processed using the same procedure applied to the 1D data. Resultant spectra are shown in Fig. 12 along with a series of 1D spectra based on the radial models (Fig. 3). Note that in computing waveforms (Yspec) and eigenfrequencies (MINEOS) gravity and attenuation are ignored. All spectra have been rescaled for comparison. This figure depicts the relative variation in the frequencies of the spectral peaks among 3D spectra determined at several stations (Fig. 12A–B) and among 1D spectra at a single station but different radial models (Fig. 12C–D). The comparison (see zoom-ins) seems to indicate that the inter-station frequency variation in the 3D spectra is smaller than the across-model variation observed in the case of 1D. This is apparent in the variation of the vertical lines, which indicates the variation in Δf . For the five spectra shown in Fig. 12A–B and Fig. 12C–D, Δf lies in the ranges 0.172–0.174 mHz (3D) and 0.166–0.177 mHz (1D), respectively. This suggests that variations in the globally-averaged structure are likely to be more significant than perturbations arising from 3D variations.

A quantitative means of assessing differences between 3D and 1D approaches would be to compare radial profiles obtained from inversion of 3D data at several locations to the profiles obtained from inversion of the average 3D model. However, because a statistically meaningful analysis implies performing inversions at many stations, which is computationally prohibitive, we rely on the following approach:

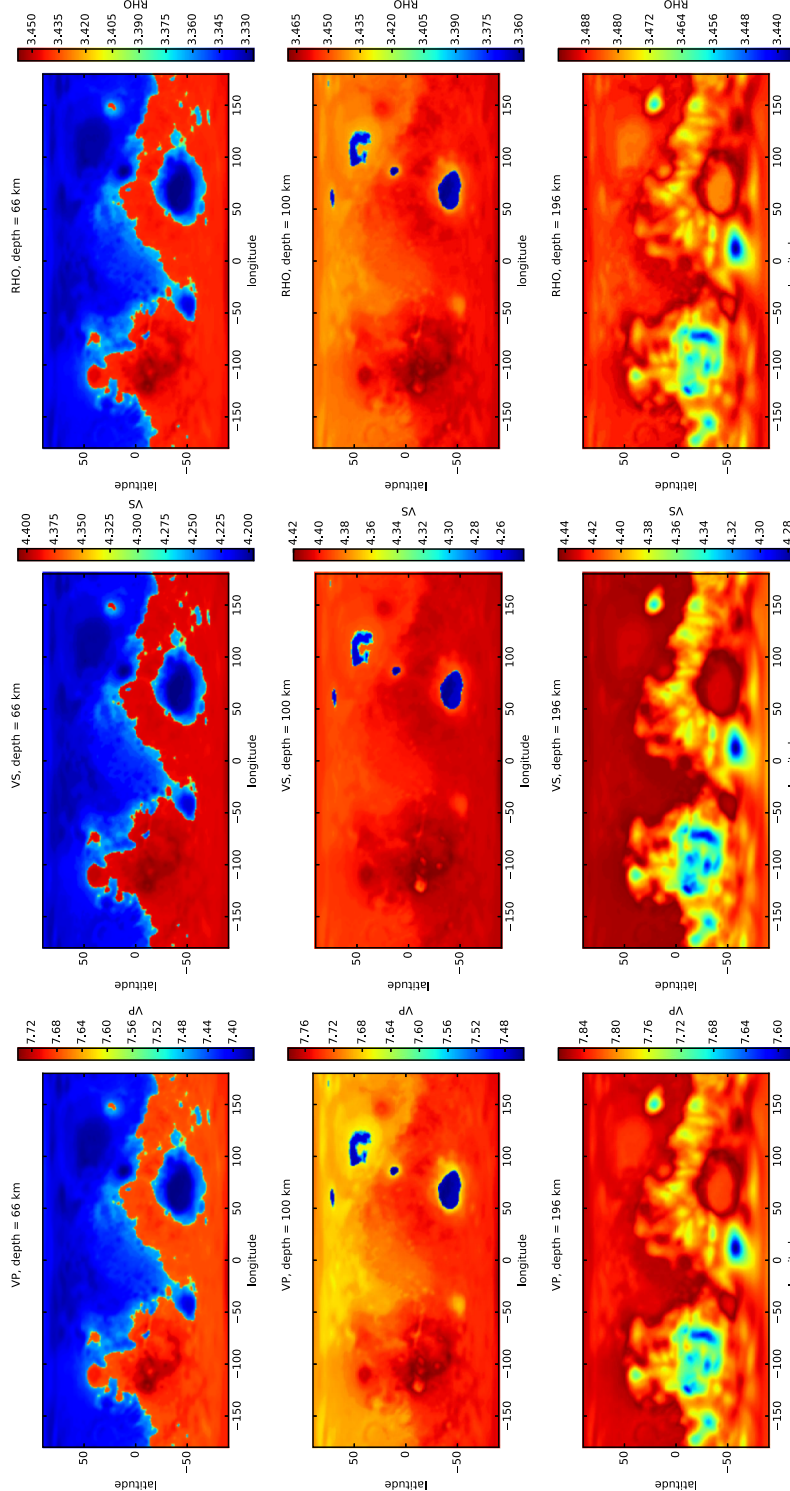


Fig. 11 Slices through a three-dimensional Martian seismic model showing lateral variations in P-wave speed (left-most panels), S-wave speed (middle panels), and density (right-most panels) in the crust and upper mantle of Mars at depths of 66, 100, and 196 km, respectively

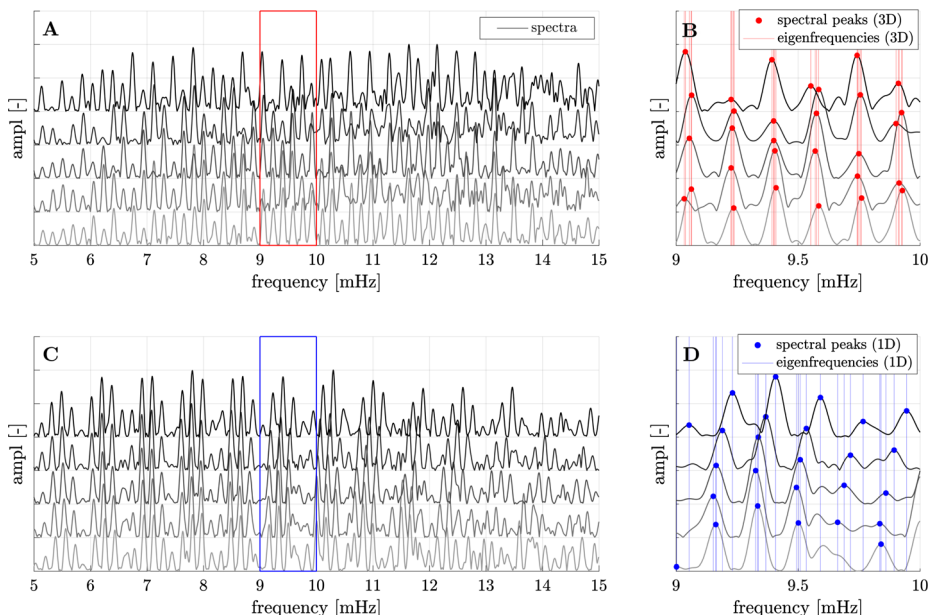


Fig. 12 Relative variation in spectral peak frequencies. (A) frequency variation among 3D spectra determined at a number of stations across the planet for the model in Fig. 11; (B) zoom-in of (A). (C) frequency variation among 1D spectra at a single station but different radial models (see Fig. 3); (D) zoom-in of (C). Vertical lines and dots in (B) and (D) indicate selected spectral peaks. Spectra are rescaled for comparison

1. Pick spectral peaks: fundamental-mode peaks in the 3D spectra are selected for 20 randomly chosen stations according to the spectral estimation scheme (Sect. 3.4);
2. Identify peak clusters: selected peaks appear to form clusters with similar frequencies in agreement with the observation of little variation in 3D spectral peak frequencies between stations as seen in Fig. 12B. As a consequence, it should be possible to find groups of peak frequencies that correspond to the same mode. A binning procedure is applied for grouping the frequencies into these clusters. The width of each bin is set to be equal to the mean value of Δf over the 20 spectra examined. Many sets of bins are tested and the squared distance of the i th frequency (f_k^i) to the mean frequency (\bar{f}_k) in a given bin k is computed from

$$\Phi = \sum_{k,i} \|f_k^i - \bar{f}_k\|^2 \quad (4)$$

- and the set of bins that minimises this function is chosen for further analysis;
3. Compute standard deviation: after having determined the bins, the standard deviation of the observed spectral peak frequencies in each bin is computed, which is interpreted as a measure of the relative spectral variation. The maximum value of this standard deviation is on the order of $\Delta f/2$ given the fixed bin-width; and
 4. Repeat steps 1–3 for the 1D-model spectra: 200 models are drawn randomly from the sampled prior (gray histograms in Fig. 10), which represent plausible Martian 1D models. For these 200 models, we compute fundamental-mode frequencies directly using MINEOS. For consistency, we keep the same binning-procedure and bin-width as in the 3D case. Finally, we compute the standard deviation for each bin.

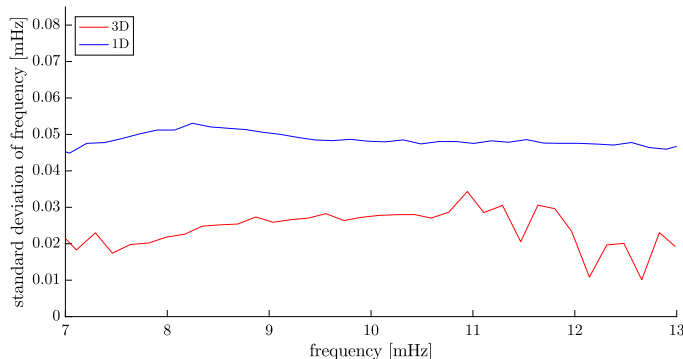


Fig. 13 Comparison of spectral variation based on globally-averaged models (Fig. 3) and a three-dimensional model (Fig. 11) as a function of frequency. The 3D frequency variation is determined by investigating how the frequency changes across a number of stations distributed over the planet based on a single 3D seismic model (Fig. 11); the 1D frequency variation is obtained by considering the frequency change at a single station but different radial models (Fig. 3)

Figure 13 summarises the variation in standard deviation as a function of frequency for both 1D and 3D cases. We limited the frequency range to 7–13 mHz, because 3D spectral peaks are too sparse above and below this frequency range. Identification of additional fundamental-mode spectral peaks might be possible after a preliminary inversion run. The figure indicates that the standard deviation and thus relative spectral variation among different 1D models is about twice as large as the standard deviation in the case of 3D. Consequently, variations in the globally-averaged structure appear to have a larger influence on fundamental-mode frequencies than the features included in our 3D model. A similar analysis conducted using a different 3D model that includes larger crustal variations confirms these conclusions (see Appendix B). In summary, 3D structure as modelled here appears not to present a limitation to our method. Models that incorporate compositional variations should be explored in the future (e.g., Baratoux et al. 2014; Bozdağ et al. 2017).

7 Summary and Conclusions

In this study, we have developed an approach for extracting information on the interior of Mars by focussing on the long-period part of the seismogram (> 60 s), where normal modes are expected to be dominant. Based on vertical-component simulations of ground-motion for a relatively large Mars quake ($M_w 5.8$), we 1) computed the amplitude-spectrum and its autocorrelation to determine the frequency spacing of the fundamental spheroidal modes; 2) identify evenly-distributed fundamental-mode spectral peaks in the frequency range 5–15 mHz and invert the spectral peak frequencies for globally-averaged models of the interior structure of Mars; 3) verify the set of peaks by either discarding and/or adding peaks based on how well the synthetic spectral peaks fit the observations; and 4) re-invert the revised spectral peak frequencies for a final set of interior models fitting the observations within their uncertainty. The method was successfully applied to a synthetic test where it was demonstrated that the “true” model could be retrieved. This test also showed that inversion of fundamental spheroidal modes in the frequency range 5–15 mHz, information is limited to the depth range 0–250 km. The method is generally formulated and can easily be extended to include short-period seismic data and other observables such as geodetic data as these are

recorded by InSight. Here, we made the simplifying assumption of uniform and fixed bulk composition. More generally, this constraint should be relaxed, preferably in combination with the addition of other data.

The choice of parameters determining the width of the synthetic peaks, although somewhat subjective, is less significant as inversions using different peak widths have shown. Increasing the width of the peaks will result in broader probability distributions, but similar mean model. In the case of low signal-to-ratio, for example, we could envision starting with relatively broad peaks and then to decrease modelled peak width iteratively in several inversion stages to improve convergence.

In this context, it is important to emphasise that the method, because of the observation of a constant frequency spacing in the fundamental spheroidal mode branch, is robust in spite of the fact that we are not properly modeling the spectral amplitudes. This can be understood as follows: let us assume that a specific peak contains contributions from a fundamental mode and an overtone. The contribution of the overtone, if located at exactly the same frequency as the fundamental mode, will act to change the amplitude of the peak. But, since we are not fitting the observed amplitudes *per se*, which would require modeling the moment tensor in addition to the seismic model, this change in amplitude is of no relevance in the inversion as we are focusing on the frequency of the peak. If, however, the overtone is slightly off in frequency, which would act to either broaden and/or slightly modify the frequency of the observed resultant peak, then this would be detected by the constant frequency-spacing analysis whereby peaks are selected in the first place. Therefore, if modified in frequency, then that particular peak would not match the observed frequency spacing coherently and thus not be singled out in the first place. It might eventually, after a preliminary inversion, reveal itself as a potential fundamental mode contaminated by signal from overtones and/or proper noise. The same arguments essentially apply in the case of low signal-to-noise ratio. First off, for very low signal-to-noise ratio, the autocorrelation would simply not yield a useable frequency spacing. For intermediate signal-to-noise ratio, we could potentially find ourselves in the situation where we initially select a noise rather than a fundamental mode peak. However, assigning peaks based on the estimated frequency spacing when moving across the spectrum would be incoherent and therefore an indication that the initially-selected peak is very likely an “outlier”. It should be clear that the procedure is dependent on data quality and will require some manual fine-tuning, but it is nevertheless the case that the use of data as a means of pre-selecting and refining models (and modes) is the strong point of the method.

We have tested a relatively large event, which is not expected to occur more than once during the nominal mission lifetime. However, it stands to reason that the method works equally well for a lower magnitude event, such as M_w 5.5 of which 1–10 are expected to occur within the 2 years of the nominal mission, and based on the currently expected signal-to-noise ratio (Fig. 1), normal modes should be detectable during nighttime for \sim 5.5 events. Moreover, in this study we adhered to a more conservative noise model, whose signal-to-noise ratio is lower than that of the recent model produced by the InSight noise model working group. As a consequence, any improvement in the signal-to-noise ratio relative to what has been implemented here, translates into an improvement of the results.

Finally, to assess the impact of 3D structure on the fundamental spheroidal modes of Mars, we first constructed 3D models of Mars’ interior and subsequently performed full 3D waveform simulations in these models. Comparison of 3D and 1D spectra showed that changes in global radial structure are more important than the lateral variations in seismic properties that were modeled here. This suggests that, to first order, our 1D analysis presents an additional and independent means for obtaining information on the interior of Mars.

Additional 3D models including plausible compositional variations across the planet will have to be investigated to test the relative importance of 1D versus 3D structure further.

Ultimately, the success of the methodology developed here for determining upper mantle structure will depend on installation characteristics of the seismometer and the hitherto unknown levels of Martian seismicity and background seismic noise. These parameters will be estimated as of the end of 2018.

Acknowledgements We thank two anonymous reviewers for comments that helped improve the manuscript. We would like to acknowledge support from the Swiss National Science Foundation (SNSF project 200021_172508). This work was also supported by a grant from the Swiss National Supercomputing Centre (CSCS) under project ID s830. Part of the computations were performed on the ETH cluster Euler. This is InSight contribution 72.

Appendix A: “Benchmark Inversion”

In the method proposed here, the computation of synthetic spectra relies on an approximation and only serves as a tool for fitting eigenfrequencies. This principally arises because of lack of knowledge of the seismic source. To quantitatively test the proposed method, we shall assume that source parameters (location and mechanism) are perfectly known and proceed to compute the “true” amplitude- and phase-spectrum. This “real spectrum” can be inverted for interior structure and the results compared to those obtained from our approximate method. For the inversion of amplitude and phase, we rely on the Bayesian approach used earlier, but 1) adjust the forward routine by including Yspec for the computation of time series for each new sampled model and 2) re-formulate the likelihood function as follows

$$\mathcal{L}(\mathbf{m}) \propto \exp\left(-\sum_i \left(\frac{|A_{\text{obs}}(\omega_i) - A_{\text{syn}}(\omega_i)|^2}{2(\sigma_i^A)^2} + \frac{|\phi_i^\vee|^2}{2(\sigma_i^\phi)^2} \right)\right) \quad (5)$$

where A_{obs} and A_{syn} denote observed and synthetic amplitude, respectively, and ϕ^\vee the angle between observed and synthetic phase, evaluated at the frequency ω_i of the observed peaks. Since all peaks are considered, this automatically includes overtones and noise alongside fundamental-mode peaks. For the purposes of this test, uncertainty in amplitude (σ^A) is set to 30% and uncertainty in phase (σ^ϕ) to $\pm 0.1\pi$. Inverting amplitude and phase for the same parameters (Moho depth and lithosphere thickness and temperature) as done previously (Sect. 5) results in the sampled posterior distributions for model and data parameters displayed in Fig. 14A–E. To ensure adequate coverage of the model space, multiple inversions starting with different initial models were run in parallel. Relative to previous results (Fig. 10A–C), sampled model variances are smaller and simply reflects inversion of a larger dataset, i.e., more information. Nevertheless, the results are generally in good agreement with those obtained from the approximate method and attests to proper performance of the latter. In addition, our approximate method is computationally much cheaper (~ 0.85 s for one forward routine on a single CPU) than the “full” approach (~ 200 s for one forward routine on a single CPU).

Appendix B: Additional 3D–1D Comparison

To additionally test the importance of 3D effects, we analyzed a second model with stronger lateral variations (S-wave speed of $\pm 5\%$) in the crust following Khan et al. (2018) on top of

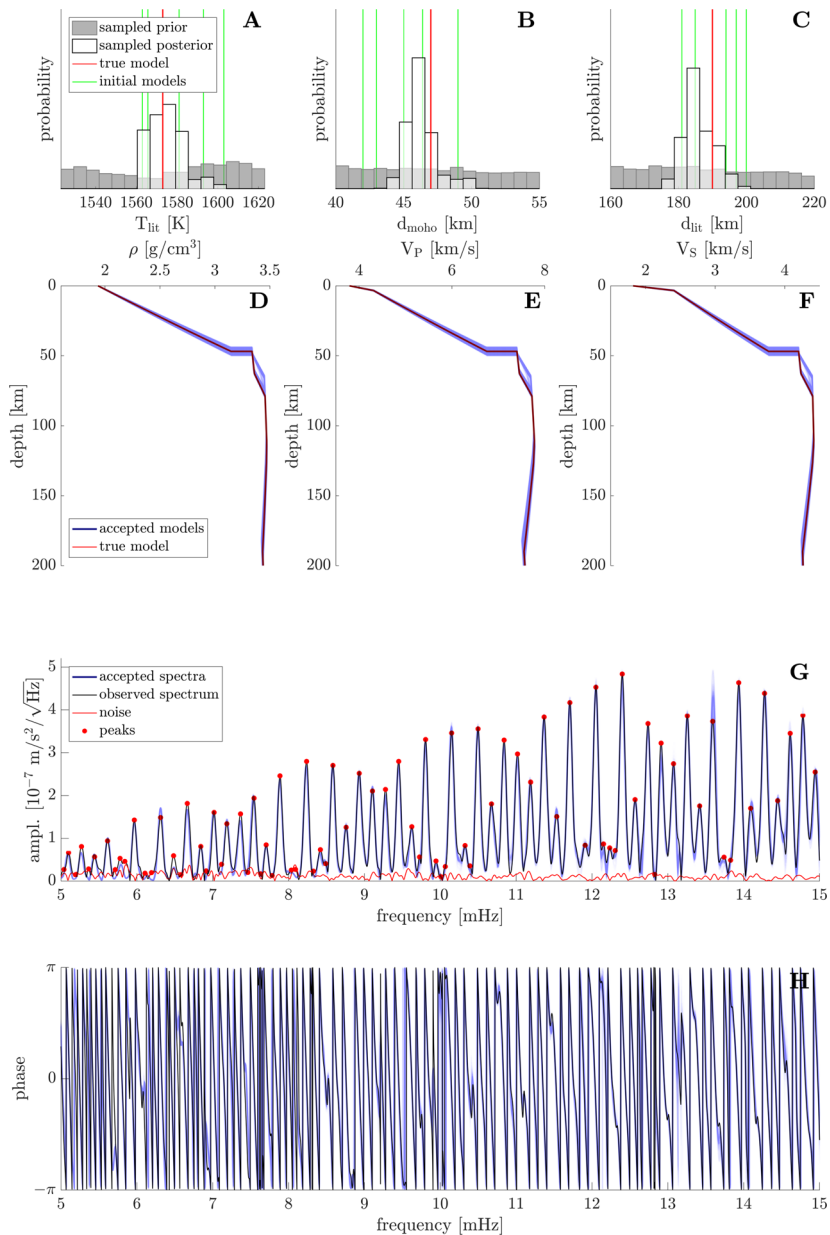


Fig. 14 Inversion results using full amplitude and phase information. **(A)-(C)** sampled prior and posterior distributions for the main crustal and lithospheric parameters of interest (temperature at the bottom of the lithosphere, Moho thickness, lithospheric thickness). **(D)-(F)** Corresponding radial profiles of density, P- and S-wave speed. **(G)-(H)** fitted amplitude **(D)** and phase **(E)** spectra. Misfit is evaluated at the frequencies indicated by the red dots

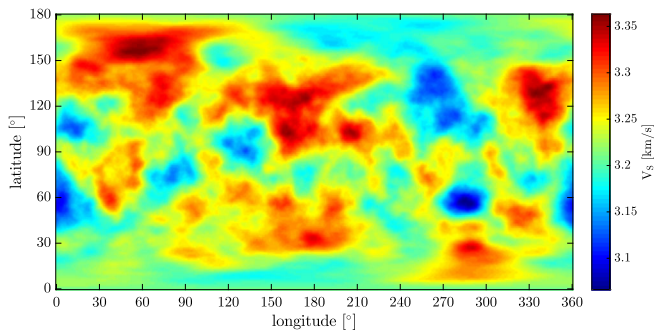


Fig. 15 Slice through a three-dimensional seismic model showing lateral variations in S-wave speed in the crust at a depth of 54 km

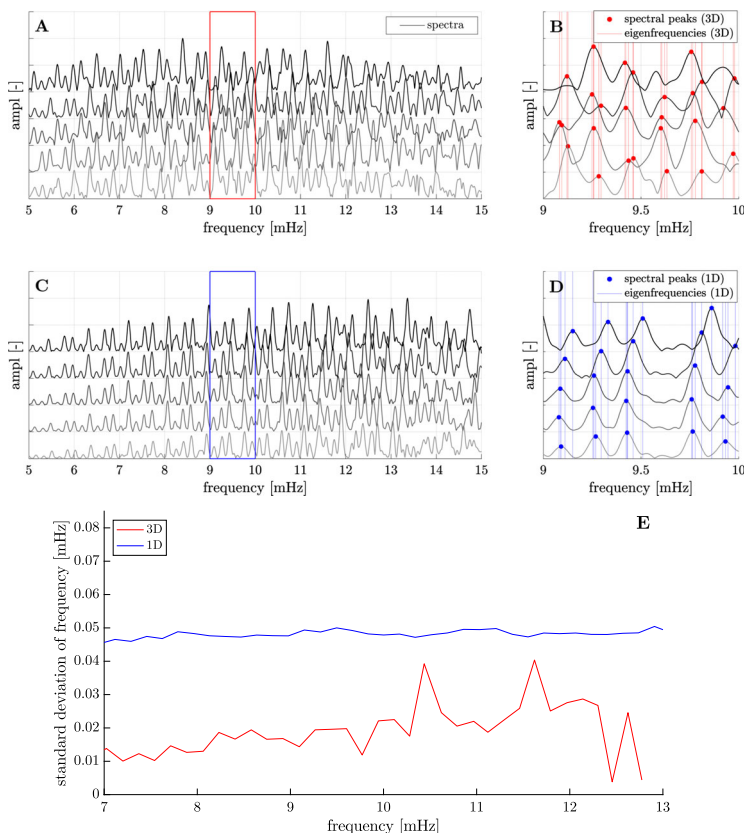


Fig. 16 (A) frequency variation among 3D spectra determined at a number of stations across the planet for the model in Fig. 15; (B) zoom-in of (A). (C) frequency variation among 1D spectra at a single station but different radial models (see Fig. 3); (D) zoom-in of (C). Vertical lines and dots in (B) and (D) indicate selected spectral peaks. Spectra are rescaled for comparison. (E) comparison of spectral variation based on globally-averaged models (Fig. 3) and a three-dimensional model (Fig. 15) as a function of frequency. The 3D frequency variation is determined by investigating how the frequency changes across a number of stations distributed over the planet based on the model in Fig. 15; the 1D frequency variation is obtained by considering the frequency change at a single station but different radial models (Fig. 3)

a 1D mantle. In this model lateral variations in the mantle are neglected because these are unlikely to be seen given the large crustal perturbations combined with decreased sensitivity at greater depth. In the crust, the ratio of S- to P-wave speed is 0.55 and the ratio of density to P-wave speed is 1.2. Repeating the analysis outlined in Sect. 6.3, 3D and 1D spectra are compared in Fig. 16A–E. While the quality of the spectra is generally worse in comparison to the previous 3D model, it is nonetheless possible to pick Δf and select fundamental-mode peaks across 20 different stations. As in the previous analysis, Δf varies between 0.169 and 0.172 and is thus of the same order as observed previously. This suggests that for the expected long-wavelength 3D variability, peak frequency variability is less important than the variability due to the range of possible 1D models.

Appendix C: Description of Supplementary Material

Additional material can be found in the Online Resource of this article. It contains figures showing 1) additionally investigated radial models, 2) corresponding dispersion curves and spacing of fundamental modes (Δf), and 3) comparison of estimated and theoretical Δf .

References

- M. Afanasiev, C. Boehm, M. van Driel, L. Krischer, M. Rietmann, D. May, M. Knepley, A. Fichtner, Salvus: A high-performance package for full waveform modelling and inversion from laboratory to global scales. *Geophys. J. Int.* (2018 submitted). ID GJI-S-17-1139
- D. Al-Attar, J.H. Woodhouse, Calculation of seismic displacement fields in self-gravitating Earth models—applications of minors vectors and symplectic structure. *Geophys. J. Int.* **175**(3), 1176–1208 (2008). <https://doi.org/10.1111/j.1365-246X.2008.03961.x>
- D.L. Anderson, W.F. Miller, G.V. Latham, Y. Nakamura, M.N. Toksoz, A.M. Dainty, F.K. Duennenbier, A.R. Lazarewicz, R.L. Kovach, T.C.D. Knight, Seismology on Mars. *J. Geophys. Res.* **82**(28), 4524–4546 (1977). <https://doi.org/10.1029/JS082i028p04524>
- W.B. Banerdt, S. Smrekar, P. Lognonné, T. Spohn, S.W. Asmar, D. Banfield, L. Boschi, U. Christensen, V. Dehant, W. Folkner, D. Giardini, W. Goetze, M. Golombek, M. Grott, T. Hudson, C. Johnson, G. Kargl, N. Kobayashi, J. Maki, D. Mimoun, A. Mocquet, P. Morgan, M. Panning, W.T. Pike, J. Tromp, T. van Zoest, R. Weber, M.A. Wieczorek, R. Garcia, K. Hurst, InSight: a discovery mission to explore the interior of Mars, in *Lunar and Planetary Science Conference*. Lunar and Planetary Institute Technical Report, vol. 44, 2013, p. 1915
- D. Baratoux, H. Samuel, C. Michaut, M.J. Toplis, M. Monnereau, M. Wieczorek, R. Garcia, K. Kurita, Petrological constraints on the density of the Martian crust. *J. Geophys. Res.* **119**(E7), 1707–1727 (2014). <https://doi.org/10.1002/2014JE004642>
- C.M. Bertka, Y. Fei, Mineralogy of the Martian interior up to core-mantle boundary pressures. *J. Geophys. Res.* **102**(B3), 5251–5264 (1997). <https://doi.org/10.1029/96JB03270>
- P. Bogiatzis, M. Ishii, Constraints on the moment tensor of the 2011 Tohoku-Oki earthquake from Earth's free oscillations. *Bull. Seismol. Soc. Am.* **104**(2), 875–884 (2014). <https://doi.org/10.1785/0120130243>
- B.A. Bolt, J.S. Derr, Free bodily vibrations of the terrestrial planets. *Vistas Astron.* **11**, 69–102 (1969)
- M. Böse, J.F. Clinton, S. Ceylan, F. Euchner, M. van Driel, A. Khan, D. Giardini, P. Lognonné, W.B. Banerdt, A probabilistic framework for single-station location of seismicity on Earth and Mars. *Phys. Earth Planet. Inter.* **262**, 48–65 (2017). <https://doi.org/10.1016/j.pepi.2016.11.003>
- E. Bozdağ, Y. Ruan, N. Metthez, A. Khan, K. Leng, M. van Driel, M. Wieczorek, A. Rivoldini, C.S. Larmat, D. Giardini, J. Tromp, P. Lognonné, W.B. Banerdt, Simulations of seismic wave propagation on Mars. *Space Sci. Rev.* **211**, 571–594 (2017). <https://doi.org/10.1007/s11214-017-0350-z>
- R.E. Carr, R.L. Kovach, Toroidal oscillations of the Moon. *Icarus* **1**(1), 75–76 (1962)
- S. Ceylan, M. van Driel, F. Euchner, A. Khan, J. Clinton, L. Krischer, M. Böse, S.C. Stähler, D. Giardini, From Initial models of seismicity, structure, and noise to synthetic seismograms for Mars. *Space Sci. Rev.* **211**, 595–610 (2017). <https://doi.org/10.1007/s11214-017-0380-6>

- J.F. Clinton, D. Giardini, P. Lognonné, W.B. Banerdt, M. van Driel, M. Drilleau, N. Murdoch, M. Panning, R. Garcia, D. Mimoun, M. Golombek, J. Tromp, R. Weber, M. Böse, S. Ceylan, I. Daubar, B. Kenda, A. Khan, L. Perrin, A. Spiga, Preparing for InSight: an invitation to participate in a blind test for Martian seismicity. *Seismol. Res. Lett.* **88**(5), 1290–1302 (2017). <https://doi.org/10.1785/0220170094>
- J.A.D. Connolly, The geodynamic equation of state: what and how. *Geochem. Geophys. Geosyst.* **10**(10), Q10014. (2009). <https://doi.org/10.1029/2009GC002540>
- F.A. Dahlen, R.V. Sailor, Rotational and elliptical splitting of the free oscillations of the Earth. *Geophys. J. Int.* **58**(3), 609–623 (1979). <https://doi.org/10.1111/j.1365-246X.1979.tb04797.x>
- V. Debaille, Q.-Z. Yin, A.D. Brandon, B. Jacobsen, Martian mantle mineralogy investigated by the ^{176}Lu – ^{176}Hf and ^{147}Sm – ^{143}Nd systematics of shergottites. *Earth Planet. Sci. Lett.* **269**(1–2), 186–199 (2008). <https://doi.org/10.1016/j.epsl.2008.02.008>
- J.S. Derr, Free oscillations of new lunar models. *Phys. Earth Planet. Inter.* **2**(2), 61–68 (1969)
- G. Dreibus, H. Wänke, Mars, a volatile-rich planet. *Meteoritics* **20**, 367–381 (1985)
- J.J. Durek, G. Ekström, A radial model of anelasticity consistent with long-period surface-wave attenuation. *Bull. Seismol. Soc. Am.* **86**(1A), 144–158 (1996)
- W.M. Folkner, S.W. Asmar, V. Dehant, R.W. Warwick, The Rotation and Interior Structure Experiment (RISE) for the InSight mission to Mars, in *Lunar and Planetary Science Conference*. Lunar and Planetary Science Conference, vol. 43, 2012, p. 1721
- J. Gagnepain-Beyneix, P. Lognonné, H. Chenet, D. Lombardi, T. Spohn, A seismic model of the lunar mantle and constraints on temperature and mineralogy. *Phys. Earth Planet. Inter.* **159**(3–4), 140–166 (2006). <https://doi.org/10.1016/j.pepi.2006.05.009>
- P. Gaulme, B. Mosser, F.-X. Schmider, T. Guillot, Seismology of giant planets, in *Extraterrestrial Seismology*, ed. by V. Tong, R. García (Cambridge University Press, Cambridge, 2015), pp. 189–202. 978-1-107-04172-1. <https://doi.org/10.1017/CBO9781107300668.017>
- F. Gilbert, A. Dziewonski, An application of normal mode theory to the retrieval of structural parameters and source mechanisms from seismic spectra. *Philos. Trans. R. Soc. Lond. A* **278**(1280), 187–269 (1975). <https://doi.org/10.1098/rsta.1975.0025>
- N.R. Goins, A.R. Lazarewicz, Martian seismicity. *Geophys. Res. Lett.* **6**(5), 368–370 (1979). <https://doi.org/10.1029/GL006i005p00368>
- M.P. Golombek, A revision of Mars seismicity from surface faulting, in *Abstracts of Papers Submitted to the Lunar and Planetary Science Conference*, vol. 33 (2002)
- M.P. Golombek, W.B. Banerdt, K.L. Tanaka, D.M. Tralli, A prediction of Mars seismicity from surface faulting. *Science* **258**(5084), 979–981 (1992). <https://doi.org/10.1126/science.258.5084.979>
- T.V. Gudkova, S.N. Raevskii, Spectrum of the free oscillations of the Moon. *Sol. Syst. Res.* **47**(1), 11–19 (2013). <https://doi.org/10.1134/S0038094613010024>
- T.V. Gudkova, V.N. Zharkov, The exploration of Martian interiors using the spheroidal oscillation method. *Planet. Space Sci.* **44**(11), 1223–1230 (1996). [https://doi.org/10.1016/S0032-0633\(96\)00124-9](https://doi.org/10.1016/S0032-0633(96)00124-9)
- T.V. Gudkova, V.N. Zharkov, The spectrum of torsional oscillations of the Moon. *Sol. Syst. Res.* **34**(6), 460–468 (2000). <https://doi.org/10.1023/A:1005214012072>
- T.V. Gudkova, V.N. Zharkov, On the excitation of free oscillations on the Moon. *Astron. Lett.* **27**(10), 658–670 (2001). <https://doi.org/10.1134/1.1404460>
- T.V. Gudkova, V.N. Zharkov, The exploration of the lunar interior using torsional oscillations. *Planet. Space Sci.* **50**(10–11), 1037–1048 (2002). [https://doi.org/10.1016/S0032-0633\(02\)00070-3](https://doi.org/10.1016/S0032-0633(02)00070-3)
- T.V. Gudkova, V.N. Zharkov, Mars: interior structure and excitation of free oscillations. *Phys. Earth Planet. Inter.* **142**(1–2), 1–22 (2004). <https://doi.org/10.1016/j.pepi.2003.10.004>
- T.V. Gudkova, V.N. Zharkov, Theoretical free oscillations spectrum for Saturn interior models. *Adv. Space Res.* **38**(4), 764–769 (2006). <https://doi.org/10.1016/j.asr.2006.02.042>
- T.V. Gudkova, V.N. Zharkov, S.A. Lebedev, Theoretical spectrum of free oscillations of Mars. *Sol. Syst. Res.* **27**, 129–148 (1993)
- T.V. Gudkova, B. Mosser, J. Provost, G. Gabrier, D. Gautier, T. Guillot, Seismological comparison of giant planet interior models. *Astron. Astrophys.* **303**, 594–603 (1995)
- T.V. Gudkova, P. Lognonné, J. Gagnepain-Beyneix, Large impacts detected by the Apollo seismometers: impactor mass and source cutoff frequency estimations. *Icarus* **211**, 1049–1065 (2011). <https://doi.org/10.1016/j.icarus.2010.10.028>
- I. Jackson, U.H. Faul, Grainsize-sensitive viscoelastic relaxation in olivine: towards a robust laboratory-based model for seismological application. *Phys. Earth Planet. Inter.* **183**(1–2), 151–163 (2010). <https://doi.org/10.1016/j.pepi.2010.09.005>
- B. Kenda, P. Lognonné, A. Spiga, T. Kawamura, S. Kedar, W.B. Banerdt, R. Lorenz, D. Banfield, M. Golombek, Modeling of ground deformation and shallow surface waves generated by Martian dust devils and perspectives for near-surface structure inversion. *Space Sci. Rev.* **211**(1), 501–524 (2017). <https://doi.org/10.1007/s11214-017-0378-0>

- A. Khan, K. Mosegaard, New information on the deep lunar interior from an inversion of lunar free oscillation periods. *Geophys. Res. Lett.* **28**(9), 1791–1794 (2001)
- A. Khan, M. van Driel, M. Böse, D. Giardini, S. Ceylan, J. Yan, J. Clinton, F. Euchner, P. Lognonné, N. Murdoch, D. Mimoun, M. Panning, M. Knapmeyer, W.B. Banerdt, Single-station and single-event marsquake location and inversion for structure using synthetic Martian waveforms. *Phys. Earth Planet. Inter.* **258**, 28–42 (2016). <https://doi.org/10.1016/j.pepi.2016.05.017>
- A. Khan, C. Liebske, A. Rozel, A. Rivoldini, F. Nimmo, J.A.D. Connolly, A.-C. Plesa, D. Giardini, A geo-physical perspective on the bulk composition of Mars. *J. Geophys. Res.* **123**(E2), 575–611 (2018). <https://doi.org/10.1002/2017JE005371>
- M. Knapmeyer, J. Oberst, E. Hauber, M. Wählisch, C. Deuchler, R. Wagner, Working models for spatial distribution and level of Mars' seismicity. *J. Geophys. Res.* **111**(E11), 1–23 (2006). <https://doi.org/10.1029/2006JE002708>
- N. Kobayashi, K. Nishida, Continuous excitation of planetary free oscillations by atmospheric disturbances. *Nature* **395**(6700), 357–360 (1998)
- C. Larmat, J.-P. Montagner, Y. Capdeville, W.B. Banerdt, P. Lognonné, J.-P. Vilotte, Numerical assessment of the effects of topography and crustal thickness on martian seismograms using a coupled modal solution spectral element method. *Icarus* **196**(1), 78–89 (2008). <https://doi.org/10.1016/j.icarus.2007.12.030>
- P. Lognonné, C. Johnson, Planetary seismology, in *Treatise on Geophysics*, ed. by G. Schubert (Elsevier, Amsterdam, 2014), pp. 69–122. 978-0-444-52748-6. <https://doi.org/10.1016/B978-044452748-6.00154-1>
- P. Lognonné, B. Mosser, Planetary seismology. *Surv. Geophys.* **14**(3), 239–302 (1993). <https://doi.org/10.1007/BF00690946>
- P. Lognonné, B. Mosser, F.A. Dahlen, Excitation of Jovian seismic waves by the Shoemaker-Levy 9 cometary impact. *Icarus* **110**(2), 180–195 (1994). <https://doi.org/10.1006/icar.1994.1115>
- P. Lognonné, J. Gagnepain-Beyneix, W.B. Banerdt, S. Cacho, J.F. Karczewski, M. Morand, Ultra broad band seismology on InterMarsNet. *Planet. Space Sci.* **44**(11), 1237–1249 (1996). [https://doi.org/10.1016/S0032-0633\(96\)00083-9](https://doi.org/10.1016/S0032-0633(96)00083-9)
- P. Lognonné, W.B. Banerdt, D. Giardini, U. Christensen, D. Mimoun, S. de Raucourt, A. Spiga, R. Garcia, A. Mocquet, M. Panning, E. Beucler, L. Boschi, W. Goetz, T. Pike, C. Johnson, R. Weber, M. Wieczorek, K. Larmat, N. Kobayashi, J. Tromp, Insight and single-station broadband seismology: from signal and noise to interior structure determination, in *Lunar and Planetary Science Conference*. Lunar and Planetary Inst. Technical Report, vol. 43, 2012, p. 1983
- P. Lognonné, F. Karakostas, L. Rolland, Y. Nishikawa, Modeling of atmospheric-coupled Rayleigh waves on planets with atmosphere: from Earth observation to Mars and Venus perspectives. *J. Acoust. Soc. Am.* **140**(2), 1447–1468 (2016). <https://doi.org/10.1121/1.4960788>
- R.D. Lorenz, Y. Nakamura, J.R. Murphy, Viking-2 seismometer measurements on Mars: PDS data archive and meteorological applications. *Earth Space Sci.* **4**(11), 681–688 (2017). <https://doi.org/10.1002/2017EA000306>
- T. Lyubetskaya, J. Korenaga, Chemical composition of Earth's primitive mantle and its variance: 1. Method and results. *J. Geophys. Res.* **112**(B3), B03211 (2007). <https://doi.org/10.1029/2005JB004223>
- G. Masters, J.H. Woodhouse, G. Freeman, 2011. Mineos v1.0.2 [software], Computational Infrastructure for Geodynamics, <https://geodynamics.org/cig/software/mineos/>
- W.F. McDonough, S.-S. Sun, The composition of the Earth. *Chem. Geol.* **120**(3–4), 223–253 (1995). [https://doi.org/10.1016/0009-2541\(94\)00140-4](https://doi.org/10.1016/0009-2541(94)00140-4)
- H.Y. McSween Jr., What we have learned about Mars from SNC meteorites. *Meteoritics* **29**, 757–779 (1994)
- W. Menke, Solution of the linear, Gaussian inverse problem, Viewpoint 1: the length method, in *Geophysical Data Analysis: Discrete Inverse Theory*, ed. by W. Menke (Elsevier, Boston, 2012), pp. 39–68. 978-0-12-397160-9
- D. Mimoun, N. Murdoch, P. Lognonné, K. Hurst, W.T. Pike, J. Hurley, T. Nébut, B. Banerdt (SEIS-Team), The noise model of the SEIS seismometer of the InSight mission to Mars. *Space Sci. Rev.* **211**(1–4), 383–428 (2017). <https://doi.org/10.1007/s11214-017-0409-x>
- K. Mosegaard, A. Tarantola, Monte Carlo sampling of solutions to inverse problems. *J. Geophys. Res.* **100**(B7), 12431–12447 (1995)
- N. Murdoch, B. Kenda, T. Kawamura, A. Spiga, P. Lognonné, D. Mimoun, W.B. Banerdt, Estimations of the seismic pressure noise on Mars determined from Large Eddy Simulations and demonstration of pressure decorrelation techniques for the Insight mission. *Space Sci. Rev.* **211**(1–4), 457–483 (2017a). <https://doi.org/10.1007/s11214-017-0343-y>
- N. Murdoch, D. Mimoun, R.F. Garcia, W. Rapin, T. Kawamura, P. Lognonné, D. Banfield, W.B. Banerdt, Evaluating the wind-induced mechanical noise on the InSight seismometers. *Space Sci. Rev.* **211**(1–4), 429–455 (2017b). <https://doi.org/10.1007/s11214-016-0311-y>

- G.A. Neumann, M.T. Zuber, M.A. Wieczorek, P.J. McGovern, F.G. Lemoine, D.E. Smith, Crustal structure of Mars from gravity and topography. *J. Geophys. Res.* **109**, E08002 (2004). <https://doi.org/10.1029/2004JE002262>
- F. Nimmo, U.H. Faul, Dissipation at tidal and seismic frequencies in a melt-free, anhydrous Mars. *J. Geophys. Res.* **118**(E12), 2558–2569 (2013). <https://doi.org/10.1002/2013JE004499>
- E.A. Okal, D.L. Anderson, Theoretical models for Mars and their seismic properties. *Icarus* **33**(3), 514–528 (1978). [https://doi.org/10.1016/0019-1035\(78\)90187-2](https://doi.org/10.1016/0019-1035(78)90187-2)
- E.A. Okal, S. Hongsresawat, S. Stein, Split-mode evidence for no ultraslow component to the source of the 2010 Maule, Chile, earthquake. *Bull. Seismol. Soc. Am.* **102**(1), 391–397 (2012). <https://doi.org/10.1785/0120100240>
- M.P. Panning, É. Beucler, M. Drilleau, A. Mocquet, P. Lognonné, W.B. Banerdt, Verifying single-station seismic approaches using Earth-based data: preparation for data return from the InSight mission to Mars. *Icarus* **248**, 230–242 (2015). <https://doi.org/10.1016/j.icarus.2014.10.035>
- M.P. Panning, P. Lognonné, W.B. Banerdt, R. Garcia, M. Golombek, S. Kedar, B. Knapmeyer-Endrun, A. Mocquet, N.A. Teamby, J. Tromp, R. Weber, E. Beucler, J.-F. Blanchette-Guerin, E. Bozdağ, M. Drilleau, T.V. Gudkova, S. Hempel, A. Khan, V. Lekić, N. Murdoch, A.-C. Plesa, A. Rivoldini, N. Schmerr, Y. Ruan, O. Verhoeven, C. Gao, U. Christensen, J. Clinton, V. Dehant, D. Giardini, D. Mimoun, W. Thomas Pike, S. Smrekar, M. Wieczorek, M. Knapmeyer, J. Wookey, Planned products of the Mars structure service for the InSight mission to Mars. *Space Sci. Rev.* **211**(1), 611–650 (2017). <https://doi.org/10.1007/s11214-016-0317-5>
- R. Phillips, Expected rate of marsquakes, in *Scientific Rationale and Requirements for a Global Seismic Network on Mars*. LPI Technical Rep., vol. 91-02 (Lunar and Planetary Institute, Houston, 1991), pp. 35–38
- A.-C. Plesa, M. Grott, N. Tosi, D. Breuer, T. Spohn, M.A. Wieczorek, How large are present-day heat flux variations across the surface of Mars? *J. Geophys. Res.* **121**(E12), 2386–2403 (2016). <https://doi.org/10.1002/2016JE005126>
- A.-C. Plesa, M. Knapmeyer, M.P. Golombek, D. Breuer, M. Grott, T. Kawamura, P. Lognonné, N. Tosi, R.C. Weber, Present-day Mars' seismicity predicted from 3-D thermal evolution models of interior dynamics. *Geophys. Res. Lett.* **45**(6), 2580–2589 (2018). <https://doi.org/10.1002/2017GL076124>
- M. Schimmel, E. Stutzmann, S. Ventosa, Low-frequency ambient noise autocorrelations: waveforms and normal modes. *Seismol. Res. Lett.* **89**(4), 1488–1496 (2018). <https://doi.org/10.1785/0220180027>
- S.C. Solomon, D.L. Anderson, W.B. Banerdt, R.G. Butler, P.M. Davis, F.K. Duennenbier, Y. Nakamura, E.A. Okal, R.J. Phillips, *Scientific Rationale and Requirements for a Global Seismic Network on Mars. Report of a Workshop* (Lunar and Planetary Institute, Houston, 1991)
- T. Spohn, M. Grott, S. Smrekar, C. Krause, T.L. Hudson (HP3 Instrument Team), Measuring the Martian heat flow using the Heat Flow and Physical Properties Package (HP3), in *Lunar and Planetary Science Conference*. Lunar and Planetary Science Conference, vol. 45, 2014, p. 1916
- L. Stixrude, C. Lithgow-Bertelloni, Thermodynamics of mantle minerals—I. Physical properties. *Geophys. J. Int.* **162**(2), 610–632 (2005). <https://doi.org/10.1111/j.1365-246X.2005.02642.x>
- L. Stixrude, C. Lithgow-Bertelloni, Thermodynamics of mantle minerals—II. Phase equilibria. *Geophys. J. Int.* **184**(3), 1180–1213 (2011). <https://doi.org/10.1111/j.1365-246X.2010.04890.x>
- G.J. Taylor, The bulk composition of Mars. *Chem. Erde* **73**(4), 401–420 (2013). <https://doi.org/10.1016/j.chemer.2013.09.006>
- S.R. Taylor, S. McLennan, *Planetary Crusts: Their Composition, Origin and Evolution* (Cambridge University Press, Cambridge, 2009)
- N.A. Teamby, J. Wookey, Seismic detection of meteorite impacts on Mars. *Phys. Earth Planet. Inter.* **186**(1–2), 70–80 (2011). <https://doi.org/10.1016/j.pepi.2011.03.004>
- A.H. Treiman, The parental magma of the Nakhla achondrite: ultrabasic volcanism on the shergottite parent body. *Geochim. Cosmochim. Acta* **50**, 1061–1070 (1986). [https://doi.org/10.1016/0016-7037\(86\)90388-1](https://doi.org/10.1016/0016-7037(86)90388-1)
- S.V. Vorontsov, V.N. Zharkov, V.M. Lubimov, The free oscillations of Jupiter and Saturn. *Icarus* **27**, 109–118 (1976)
- V.N. Zharkov, T.V. Gudkova, A.V. Batov, On estimating the dissipative factor of the Martian interior. *Sol. Syst. Res.* **51**(6), 479–490 (2017). <https://doi.org/10.1134/S0038094617060089>
- Y. Zheng, F. Nimmo, T. Lay, Seismological implications of a lithospheric low seismic velocity zone in Mars. *Phys. Earth Planet. Inter.* **240**, 132–141 (2015). <https://doi.org/10.1016/j.pepi.2014.10.004>